

國立陽明交通大學

機器人碩士學位學程

碩士論文

Graduate Degree Program of Robotics

National Yang Ming Chiao Tung University

Master Thesis

基於無損卡爾曼濾波與非線性控制器之無人機馬達效率估

測與控制

Motor Efficiency Estimation and Control of Multirotors Based

On Unscented Kalman Filter and Geometric Tracking

Controller

研究生: 張家誠 (Chia-Cheng Chang)

指導教授: 程登湖 博士 (Teng-Hu Cheng)

中華民國一百一十一年九月

September, 2022

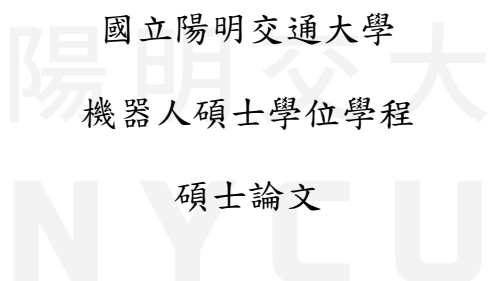
陽明交大
NYCU

基於無損卡爾曼濾波與非線性控制器之無人機馬達效率估
測與控制

Motor Efficiency Estimation and Control of Multirotors Based
On Unscented Kalman Filter and Geometric Tracking
Controller

研究生： 張家誠
指導教授： 程登湖 博士

Student : Chia-Cheng Chang
Advisor : Dr. Teng-Hu Cheng



A Thesis
Submitted to Graduate Degree Program of Robotics
College of Engineering
National Yang Ming Chiao Tung University
in partial Fulfillment of the Requirements
for the Degree of
Master of Graduate Degree Program of Robotics
in
College of Engineering

September, 2022

Taiwan, Republic of China

中華民國一百一十一年九月

陽明交大
NYCU

Acknowledgment

I would like to thank the following people, without whom I would not have been able to complete this research, and without whom I would not have made it through my master's degree!

1. The NCRL Lab. at National Yang Ming Chiao Tung University, especially to my advisor Dr. Teng-Hu Cheng, whose insight and knowledge into the subject matter steered me through this research.
2. Eason Huang, who showed me how to efficiently debug the hardware problem during the experiment and offered a lot of opinions about the design of the experiment.
3. Lioujgay, who carefully heard the problem that I faced, and gave me other useful perspectives to my research.
4. Huan Boa, who helped me check the bugs in the algorithm, and discussed the detail in UKF, including the model and observability.
5. TH Liu, who taught me how to arrange the structure of my code and fixed the simulation environment conflict. He also gave me the faith to face the problem.
6. JoJo Chen, who was good at coordinate transformations, and always willing to figure out the coordinate promblem with me.
7. Dr. Wang, who was my experiment partner. By our experiment related communication, I often received much helpful information and inspiration. Also, he shared the workload with me, which speeded up the progress of my research work.
8. Fan Andrew and WangMahua, who are always willing to help me no matter on experiments or life. We share life experience and support each other all the time.
9. BelieveLove, my senior sister in the lab, listened to my complaint and relieve me of my bad mood by her fantastic piano music.
10. Others in the lab, who have supported me when I was down, and put up with my temper for the past two years of study.
11. My family, who have been giving me all the care, trust and support.

基於無損卡爾曼濾波與非線性控制器之無人機馬達效率估測與控制

學生：張家誠

指導教授：程登湖 博士

國立陽明交通大學工學院機器人碩士學位學程碩士班

摘要

本篇論文試著提升無人機在升力打折情況下的飛行表現，升力打折的情況有很多，例如：馬達的缺陷和變形的螺旋槳等。為此，本篇論文首先藉由無損卡爾曼濾波估測出無人機的各顆馬達的升力效率，並設計出的 high gain geometric tracking controller 接受升力效率的回授，無論是升力打折又或者是回授估測出的升力效率，都將被當成不確定性，對飛行造成一致最終有界 (uniformly ultimately bounded) 的影響，但不影響穩定性。下文中，除了提供上述設計細節外，也藉由數學證明了控制器的穩定性，以及無損卡爾曼濾波的可觀性。最後會透過模擬以及實驗，展現此架構下的飛行表現。

關鍵字：多軸無人機、無人機容錯控制、幾何追蹤控制、系統參數估測、無損卡爾曼濾波

Motor Efficiency Estimation and Control of Multirotors Based On Unscented Kalman Filter and Geometric Tracking Controller

Student : Chia-Cheng Chang

Advisor : Dr. Teng-Hu Cheng

Graduate Degree Program of Robotics of
National Yang Ming Chiao Tung University

ABSTRACT

A controller based on geometric tracking controller has been developed for controlling a multirotor unmanned aerial vehicle with defective thrust system. The defective thrust can be caused by many reasons, such as defective motors and deformed propellers. To improve the flight performance of the multirotor with defective thrust system, knowing efficiency of thrust on each motor is necessary in this research and it is estimated by UKF. With estimated efficiency of thrust on each motor, the designed controller can get the estimated efficiency of thrust as feedback from the UKF estimator and improve the flight performance of the multirotor with defective thrust system. Noted that defective thrust and the feedback of estimated efficiency of thrust are all treated as an uncertainty and will cause uniformly ultimately bounded(UUB) in the controller during flight. A stability analysis was conducted to ensure that with an uncertainty the tracking errors would not diverge and the observability of UKF model was proven. By designing the UKF estimator and high gain geometric tracking controller, the flight performance has been verified in simulations and experiments.

Keywords: multirotor unmanned aerial vehicle, fault-tolerant control of the multirotor, geometric tracking controller, parameters estimation, unscented kalman filter

Table of Contents

摘要	i
Abstract	ii
Table of Contents	iii
List of Figures	vi
List of Tables	viii
1 Introduction	1
1.1 Background	1
1.2 Motivation	1
1.3 Related Works	2
1.3.1 Estimate Motors Efficiency of the Multirotor	2
1.3.2 Fault tolerant control (FTC)	2
1.4 Contributions	4
2 Problem Formulation	5
2.1 The Multirotor Dynamics with Fault	5
2.2 The Cooperative Transporstation System (CTS) Dynamics with Fault	7
2.3 Control Distribution of CTS	8
2.4 Scenario	10
2.4.1 A Motor efficiency definition	10
2.4.2 Assumption	11
2.5 Tracking Errors and Estimate Errors	11
2.6 Control Objectives	12
3 Motors Efficiency Estimation	13
3.1 Unscented Kalman Filte (UKF)	13
3.2 The Multirotor UKF Model	14

3.2.1	The predict model of the multirotor	14
3.2.2	The measurement model of the multirotor	17
3.3	The cooperative transportation system(CTS) UKF Model	17
3.3.1	The multirotors kinematics related to the CTS system	18
3.3.2	The Physical Specifications of the CTS	18
3.3.3	The dynamics of the independent multirotor in CTS	19
3.3.4	The dynamics of the independent payload in CTS	20
3.3.5	The predict model of the CTS	21
3.3.6	The measurement model of the CTS	24
3.4	UKF Observability	24
4	Controller Design	26
4.1	Translational Controller for the Multirotor	26
4.2	Rotational Controller for the Multirotor	27
4.3	Reconfiguration with Feedback Motor Efficiency	28
4.4	Closed-Loop Error System	29
4.4.1	Translational Dynamics	29
4.4.2	Rotational Dynamics	30
5	Stability Analysis	31
5.1	Stability Analysis of the Rotational Dynamics	31
5.2	Stability Analysis of the Translational Dynamics	35
5.3	Stability Analysis of the Overall System	40
6	Simulations	42
6.1	The multirotor	42
6.1.1	Setup and Ground Truth	42
6.1.2	Results	44
6.2	The Cooperative Transportation System	53
6.2.1	Setup and Ground Truth	53
6.2.2	Result	56
7	Experiments	64
7.1	The Multirotor	64

7.1.1	Hardware Architecture	64
7.1.2	Trajectory Generation	65
7.1.3	Estimate of the Motors Efficiency	66
7.1.4	Tracking Performance	68
7.2	The CTS	70
7.2.1	Hardware Architecture	71
7.2.2	Tracking Performance	72
8	Conclusion	74
References		75



List of Figures

1	Coordinate systems of four-rotor multirotor	5
2	Coordinate systems of the cooperative transportation system	7
3	UKF Coordinate systems of four-rotor multirotor	14
4	Sensor position of the cooperative transportation system	17
5	Mechanical analysis of the independent multirotor in CTS	19
6	Mechanical analysis of the independent payload in CTS	20
7	UKF Coordinate systems of the cooperative transportation system	21
8	Control Flow	26
9	Feedback Efficiency Control Flow	28
10	The multirotor model in Simscape. Noted that the yellow line is visualized trajectory and the transparent ball is a visualized waypoint.	43
11	3D trajectory for the multirotor. Noted that the yellow line is visualized trajectory, the transparent ball is a visualized waypoint, the multirotor is initially stationary on the ground with H, the colorful concentric circles is the end waypoint projection on the ground.	45
12	Position error	46
13	Velocity error	47
14	Attitude error	48
15	Angular velocity	49
16	Estimates of the motors efficiency.	50
17	Thrust command for the motors	51
18	Comparison of the position with and without the Motors Efficiency Feedback. .	52
19	The multirotor model in Simscape. Noted that the yellow line is visualized trajectory and the transparent ball is a visualized waypoint.	53
20	3D trajectory for the CTS. Noted that the yellow line is visualized trajectory, the transparent ball is a visualized waypoint, the CTS is initially stationary on the ground with H, the colorful concentric circles is the end waypoint projection on the ground.	56

21	The CTS position error	57
22	Velocity error	58
23	Attitude error	59
24	Angular velocity	60
25	Estimates of the q ₁ motors efficiency	61
26	Estimates of the q ₂ motors efficiency	62
27	Comparison of the position with and without the Motors Efficiency Feedback. .	63
28	The Multirotor Hardware architecture.	65
29	The fault condition of the motors efficiency	67
30	Estimates of the motors efficiency of the multirotor in the experiments. The dotted line represents the ground truth.	68
31	Tracking performance of the 2D position	69
32	Tracking performance of the position <i>X</i> direction.	69
33	Tracking performance of the position in <i>Z</i> direction.	70
34	Thrust Command	70
35	The CTS Hardware architecture.	71
36	Tracking performance of the 2D position	72

List of Tables

1	Definition of the multirotor symbols	5
2	Definition of the cooperative transportation system symbols	8
3	UKF symbol of the multirotor	15
4	UKF symbol of the cooperative transportation system	22
5	Ground truth motors efficiency in the Simscape simulations	43
6	Control gains used in the Simscape simulations	43
7	Covariance of process in the multirotor UKF model in the Simscape simulations	44
8	Covariance of measurement in the multirotor UKF model in the Simscape simulations	44
9	Physical parameters of the multirotor in the Simscape simulations	44
10	The CTS Ground truth motors efficiency in the Simscape simulations	54
11	Control gains used in the Simscape simulations	54
12	Covariance of process in the CTS UKF model in the Simscape simulations . . .	55
13	Covariance of measurement in the CTS UKF model in the Simscape simulations	55
14	Physical parameters of the CTS in the Simscape simulations	55
15	Parameters used in the experiments	65
16	Control gains used in the experiments	65
17	Parameters used in the experiments	72
18	Control gains used in the experiments	72

Chapter 1 Introduction

1.1 Background

A multirotor has four rotors is a underactuated mechanical system (UMS). It has six degrees of freedom (DOF) to be controlled, but has only four motors to exert force and torque on itself. Contrast to a fixed-wing aircraft [1], a multirotor doesn't need a runway to take off. It's a vertical take-off-and-landing unmanned aerial vehicle which has several potential like portability, agility and mobility. The advantages of a multirotor have resulted in various applications including search and rescue [2], agriculture [3], military attack [4] and cooperative transportation [5]. Numerous control related researches have studied how to control a multirotor robustly, including PID control and feedback linearization [6], [7], adaptive control [8], [9], sliding mode control (SMC) [10], [11], [12], model predict control [13] and geometric tracking control [14] which developed on $SO(3)$, thus avoiding the singularities of Euler angles and it guaranteed stability by Lyapunov stability theorem when the initial attitude error is less than 90° .

1.2 Motivation

One of seniors in the lab did the research about Parameter Estimation and Control of Multi-rotors Using Integral Concurrent Learning. The research estimates mass and moment of inertia of a multirotor, and feedbacks the estimation parameter for better flight control. The research experiment shows the validity of the theory when the battery is fully charged. However, when the battery voltage is getting lower, the estimated mass in the experiment is getting bigger .This is because the low voltage battery doesn't have enough voltage to actuate the motors and other elements on multirotor. The situation is reasonable because my senior doesn't put the battery power model in his research. As mentioned above, the unmodeled hardware effect does influence the research, but there was no qualitative and quantitative analysis to not ideal hardware effect in that research. Eventually, motors on a multirotor were selected as this research subject.

1.3 Related Works

1.3.1 Estimate Motors Efficiency of the Multirotor

The present work has developed the UKF model which is able to estimate the motors efficiency during multirotor flight, and the estimation method is classified into model predict estimation. There are two principal reasons to show this application is important. First, the motors efficiency estimation of the multirotor gives the researchers more detail information of the fault motors. According to the information, the researchers could estimate the flight limit of the multirotor with fault motors, and replan the flight mission to a simple one. Second, discovering the level of the motors damage prevents researchers from confusing some research problem is contributed by a new algorithm or new technique, because there is a chance that the problem is simply caused by the defective motors. Many researches have developed on the scenarios like controlling or detecting a multirotor with a broken motor [15],[16], but few researches estimate total motors efficiency on a multirotor except for [17] and [18]. In [17], to estimate the efficiency of all motors on a quadrotor, the author first builded the dynamics of multirotor with fault and discretized the linear control system. Then, the author designed the states vector and measurements of the motors efficiency estimator and proved the stability of the estimator with Lyapunov analysis and theory. Although the estimation of the motors efficiency roughly matched the ground truth value, it still had about 15% estimation error. In addition, the estimator in [17] was linear, which meant the research had linearized the highly nonlinear system. On the other hand, the present work designs the UKF model which is suitable for nonlinear system to estimate the motors efficiency. In [18], the author succeeded to estimate the motors efficiency of a quadrotor by UKF and Moving Horizon Estimation (MHE) methods, and both estimators effectiveness were validified through simulation. However, the dynamics of a quadrotor was simplified to hovering maneuver, which might lead to estimate error when the quadrotor moved too fast, and the detail UKF model was omitted in the research.

1.3.2 Fault tolerant control (FTC)

The prime objective of the FTC is to maintain the controller stability when the system undergoes failures such as hardware broken, wind disturbance and uncertainty. The studies of FTCs have developed for more than 30 years, and there were numerous researchers put their effort into them. A FTC is often divided into two categories: passive FTCs and active FTCs.

The passive FTCs are featured in their robust control characteristic. A fault in passive FTCs is usually treated as disturbance or a model uncertainty. The stability in those FTCs is mostly guaranteed by Lyapunov analysis and theory. There were many developed passive FTCs such as sliding mode control (SMC), H_∞ control [19] and adaptive control. On the other hand, the active FTCs include a variety of methods in order to conquer the system failures, such as fault detection and diagnosis (FDD) [20], [21], control reconfiguration [22] and trajectory replanning [23]. With those positive aforementioned methods, the active FTCs usually defeat the passive FTCs on most flight performance in the specific scenario. However, active FTCs can only deal with the certain problem, and have little tolerance on other failures. On this perspective, passive FTCs usually defeat active FTCs in extensive fault tolerance. The principal control objectives in the present work mostly matches with [17]. In the research active FTC [17], the author adopted a cascaded proportional-integral-derivative (PID) control, and defined the motors fault variable in control input. After the estimator detected the motors fault, the FTC provided control reconfiguration, and sacrificed heading angle command. In contrast, the present work adopted nonlinear control method with stability analysis to deal with the highly nonlinear multirotor dynamics, and the yaw angle was controlled despite the motors fault. In [18], the author adopted Model Predictive Control (MPC). MPC minimized a objective cost function subject to dynamical constraints to obtain a stabilizing control signal at each time step. Further, MPC was one of the few methodologies that can be used to design feedback control for nonlinear dynamical systems taking into consideration of actuator saturation. In addition to the active FTCs, there are numerous intelligent passive FTCs are based on sliding mode control (SMC) [24], [25], and they were developed to solve the uncertainties, unmodeled variables and disturbances. The SMCs have high compatibility so that they are capable to be compatible with other techniques including adaptive control and backstepping control. The aforementioned SMC researches demonstrate the trajectory tracking performance and robustness under disturbances via simulation, which ensure the effectiveness of resisting disturbances and the flight performance is great. Besides, the stability analysis of the SMCs are rigorously proved according to the Lyapunov analysis and theory. However, they experience the unfavorable problem of oscillations with finite amplitude and frequency, that is chattering problem. The chattering problem is caused by two primary reasons, fast dynamics and the use of digital controllers with finite sampling time. Chattering is a harmful phenomenon because it leads to low control accuracy, high wear of moving mechanical parts and high heat losses in power circuits. Therefore, the chattering problem is an

major obstacle for SMCs implementation. To deal with those negative effects on SMCs, the researchers of SMCs have developed some new techniques. Taking [26] for example, this new type of SMC maintains the advantages including high precision tracking performances and good robustness against various external disturbances. Furthermore, it has solved the chattering problem. Though the simulation has been conducted, the experiment haven't yet. On the other hand, the present work doesn't have the chattering problem, which can be confirmed by Fig. 34 and the effectiveness is proved in experiment.

1.4 Contributions

This research has developed the UKF model to estimate the motors efficiency of a multirotor and the cooperative transportation system. The new designed controller based on geometric tracking controller can endure the disturbance caused by the defective motors and the error of feedback motors efficiency. Though the defective motors lead to more translational and rotational error, the feedback estimated motors efficiency significantly reduce the error during flight. That is to say the performance of the flight is improved when the motors of the multirotor is defective.

The main contributions of this study are summarized as follows:

1. The UKF model to estimate the motors efficiency is designed for the multirotor and the CTS, and the observability is proved.
2. The developed high gain geometric tracking controller can endure the disturbance caused by defective motors and the feedback motors efficiency error, and is proved in stability analysis.
3. The flight performance is improved after the feedback of the motors efficiency, which is presented in simulation and experiment.

Chapter 2 Problem Formulation

2.1 The Multirotor Dynamics with Fault

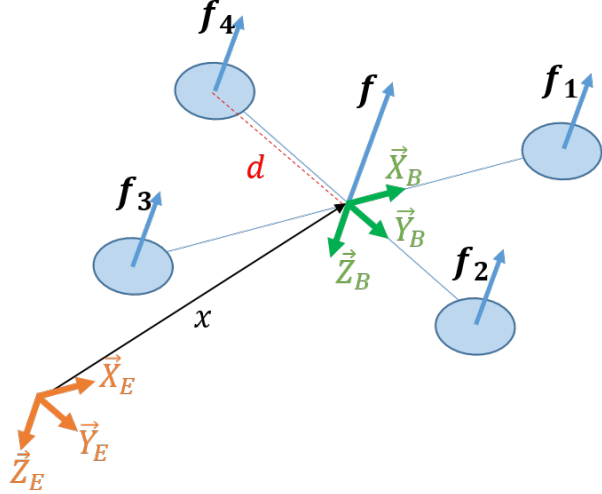


Figure 1: Coordinate systems of four-rotor multirotor

Multirotor Symbol	Description
$x \in \mathbb{R}^3$	position in the inertial frame
$v \in \mathbb{R}^3$	velocity in the inertial frame
$R \in \text{SO}(3)$	rotation matrix from the body-fixed frame to the inertial frame
$\Omega \in \mathbb{R}^3$	angular velocity in the body-fixed frame
$f \in \mathbb{R}$	thrust in the body-fixed frame
$f_j \in \mathbb{R}$	thrust generated by the j^{th} propeller
$M \in \mathbb{R}^3$	total moment in the body-fixed frame
$m \in \mathbb{R}$	mass
$d \in \mathbb{R}$	distance between the center of mass and the center of the propeller
$J \in \mathbb{R}^{3 \times 3}$	inertia matrix
$D_T \in \mathbb{R}^3$	the disturbance of thrust
$D_M \in \mathbb{R}^3$	the disturbance of moment

Table 1: Definition of the multirotor symbols

As shown in Fig. 1, the inertial frame and body-fixed frame are defined as $\{ \vec{X}_E, \vec{Y}_E, \vec{Z}_E \}$ and $\{ \vec{X}_B, \vec{Y}_B, \vec{Z}_B \}$ respectively.

The dynamics of the multirotor can be divided into two parts: translational and rotational dynamics. The translational dynamics considers forces such as the effects of gravity, the thrust of the control input, and external forces which caused by defective motors on the multirotor and the

feedback estimated motors efficiency error, and the rotational dynamics considers the moment of the control input, rotational speed, and external moment which is caused by the defective motors and the feedback estimated motors efficiency error. The dynamics of the multirotor is formulated as

$$\dot{x} = v, \quad (1)$$

$$m\dot{v} = mge_3 - (f - D_T)Re_3, \quad (2)$$

$$\dot{R} = R\hat{\Omega}, \quad (3)$$

$$J\dot{\Omega} = (M - D_M) - \Omega \times J\Omega, \quad (4)$$

where $x, v \in \mathbb{R}^3$ represent the position and velocity in the inertial frame, respectively, and $f \in \mathbb{R}$ and $M \in \mathbb{R}^3$ are thrust and moment control inputs, respectively, in the body-fixed frame. $R \in SO(3)$ is the rotation matrix from the body-fixed frame to the inertial frame, as shown in Fig. 1. m and $g \in \mathbb{R}$ are mass of the multirotor and gravity, respectively, e_3 is a unit vector defined as $e_3 = [0, 0, 1]^T \in \mathbb{R}^3$, $\Omega \in \mathbb{R}^3$ is defined as the angular velocity of the multirotor, $\dot{\Omega} \in \mathbb{R}^3$ is the angular acceleration of the multirotor, $J \in \mathbb{R}^{3 \times 3}$ is inertia matrix of the multirotor, $D_T \in \mathbb{R}$ is the disturbance of thrust and $D_M \in \mathbb{R}^3$ is the disturbance of moment. Both disturbance is caused by defective motors and the feedback estimated motors efficiency error introduced in 4.3.

The notations of the symbols are presented in Table 1. In a four-rotor multirotor, the first and third propellers rotate clockwise, and the second and fourth propellers rotate counterclockwise. The total moment generated by the propellers in the body-fixed frame is defined as

$$M \triangleq \begin{bmatrix} M_x \\ M_y \\ M_z \end{bmatrix} = \begin{bmatrix} d(f_4 - f_2) \\ d(f_1 - f_3) \\ c_{\tau f}(-f_1 + f_2 - f_3 + f_4) \end{bmatrix},$$

where f_j is the desired thrust generated by the j^{th} propeller along the $-\vec{Z}_B$ axis and can be obtained from (5) given f and M , $d > 0$ is the distance between the center of mass and the center of a propeller, and $c_{\tau f} > 0$ is a constant parameter of the propeller. The relation between

f , M , and f_j can be expressed through the allocation matrix as

$$\begin{bmatrix} f \\ M_x \\ M_y \\ M_z \end{bmatrix} = \begin{bmatrix} 1 & 1 & 1 & 1 \\ 0 & -d & 0 & d \\ d & 0 & -d & 0 \\ -c_{\tau f} & c_{\tau f} & -c_{\tau f} & c_{\tau f} \end{bmatrix} \begin{bmatrix} f_1 \\ f_2 \\ f_3 \\ f_4 \end{bmatrix}. \quad (5)$$

Remark 1. Note that the dynamics defined by (1) – (4) can be extended to multirotors with different numbers of axes by replacing the allocation matrix.

2.2 The Cooperative Transporstation System (CTS) Dynamics with Fault

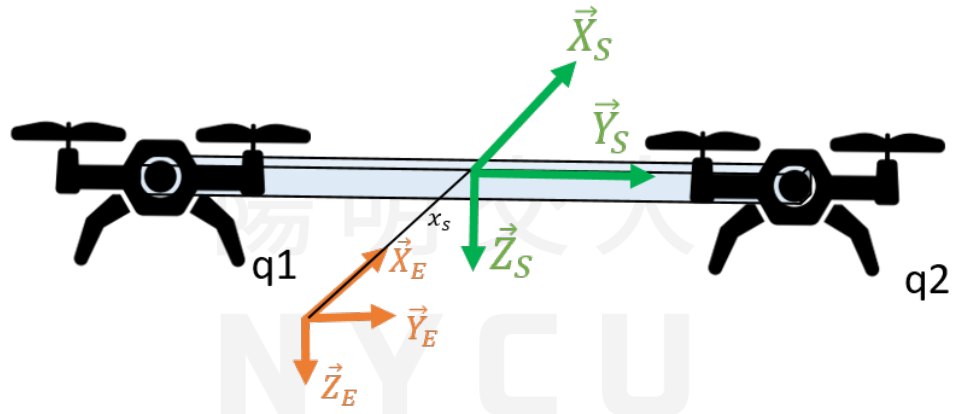


Figure 2: Coordinate systems of the cooperative transportation system

As shown in Fig. 2, the inertial frame and body-fixed frame are defined as $\{\vec{X}_E, \vec{Y}_E, \vec{Z}_E\}$ and $\{\vec{X}_S, \vec{Y}_S, \vec{Z}_S\}$ respectively.

$$\dot{x}_s = v_s, \quad (6)$$

$$m_s \dot{v}_s = m_s g e_3 - (f_s - D_{T,s}) R_s e_3, \quad (7)$$

$$\dot{R}_s = R_s \hat{\Omega}_s, \quad (8)$$

$$J_s \dot{\Omega}_s = (M_s - D_{M,s}) - \Omega_s \times J_s \Omega_s, \quad (9)$$

where $x_s, v_s \in \mathbb{R}^3$ represent the position and velocity in the inertial frame, respectively, and $f_s \in \mathbb{R}$ and $M_s \in \mathbb{R}^3$ are desired thrust and moment control inputs, respectively, in the body-fixed frame. $R_s \in \text{SO}(3)$ is the rotation matrix from the body-fixed frame to the inertial frame,

CTS Symbol	Description
$x_s \in \mathbb{R}^3$	position in the inertial frame
$v_s \in \mathbb{R}^3$	velocity in the inertial frame
$R_s \in \text{SO}(3)$	rotation matrix from the body-fixed frame to the inertial frame
$\Omega_s \in \mathbb{R}^3$	angular velocity in the body-fixed frame
$f_s \in \mathbb{R}$	total thrust in the body-fixed frame
$f_{i,s} \in \mathbb{R}$	thrust generated by the i^{th} multirotor in CTS
$M_s \in \mathbb{R}^3$	total moment in the body-fixed frame
$M_{i,s} \in \mathbb{R}^3$	moment generated by the i^{th} multirotor in CTS
$m_s \in \mathbb{R}$	mass of the system
$J_s \in \mathbb{R}^{3 \times 3}$	inertia matrix
$r \in \mathbb{R}$	the distance between the origin of the CTS and the multirotors
$D_{T,s} \in \mathbb{R}^3$	the disturbance of thrust
$D_{M,s} \in \mathbb{R}^3$	the disturbance of moment

Table 2: Definition of the cooperative transportation system symbols

as shown in Fig. 2. m_s and $g \in \mathbb{R}$ are mass of the CTS and gravity, respectively, e_3 is an unit vector defined as $e_3 = [0, 0, 1]^T \in \mathbb{R}^3$, $\Omega_s \in \mathbb{R}^3$ is defined as the angular velocity of the CTS, $\dot{\Omega}_s \in \mathbb{R}^3$ is the angular acceleration of the multirotor, and $J_s \in \mathbb{R}^{3 \times 3}$ is inertia matrix of the multirotor. The subscript s means the CTS.

2.3 Control Distribution of CTS

The thrust and moment of the CTS are generated by the two multirotors in the CTS, the relationship between f_s, M_s and $f_{i,s}, M_{i,s}$ are described as

$$u_s = \Gamma u_c \quad (10)$$

where $u_s \in \mathbb{R}^4$ is desired control input of the CTS, $\Gamma \in \mathbb{R}^{4 \times 8}$ is structure matrix, $u_c \in \mathbb{R}^8$ is control input container. They are defined as

$$u_s = \begin{bmatrix} f_s \\ M_s \end{bmatrix} \quad (11)$$

$$\Gamma = \begin{bmatrix} 1 & 0 & 0 & 0 & 1 & 0 & 0 & 0 \\ r & 1 & 0 & 0 & -r & 1 & 0 & 0 \\ 0 & 0 & 1 & 0 & 0 & 0 & 1 & 0 \\ 0 & 0 & 0 & 1 & 0 & 0 & 0 & 1 \end{bmatrix} \quad (12)$$

$$u_c = \begin{bmatrix} f_{1,s} \\ M_{1,s} \\ f_{2,s} \\ M_{2,s} \end{bmatrix} \quad (13)$$

From the flight application point of view, u_s is first calculated by controller, and then distributed to the control input container u_c of the multirotors in the CTS. Afterwards, each multirotor control input $(f_{i,s}, M_{i,s})$ would be distributed via (5) again, and the motors receive command. The CTS control input has only four variables (11), but it's distributed to the control input of the two multirotors, eight variables (13), which causes underdetermined. Therefore, each multirotor control input $(f_{i,s}, M_{i,s})$ has to be carefully chosen to achieve forces and moments u_s on the CTS. Here, $u_c^* \in \mathbb{R}^8$ represents optimal control input container which achieves the desired net force and moments u_s while minimizing the cost function $J(u_c) : \mathbb{R}^8 \rightarrow \mathbb{R}$.

u_c^* is defined as

$$u_c^* = \underset{u_c}{\operatorname{argmin}} \{ J | u_s = \Gamma u_c \}$$

where

$$J(u_c) = \sum_{i=1}^2 a_{f,i} f_{i,s}^2 + a_{M_x,i} M_{x,i}^2 + a_{M_y,i} M_{y,i}^2 + a_{M_z,i} M_{z,i}^2$$

, $M_{i,s} = [M_{x,i} \ M_{y,i} \ M_{z,i}]^T$ and $a_{(.)}$ is the coefficient of the cost function $J(u_c)$.

A natural way to treat the point-wise minimization of the cost function $J(u_c)$ is by choosing control inputs using the Moore-Penrose inverse. First we define $H \in \mathbb{R}^{8 \times 8}$ so that $J(u_c) = \|Hu_c\|_2^2$, and H is defined as

$$H = \text{diag}(\sqrt{a_{f,1}}, \sqrt{a_{M_x,1}}, \sqrt{a_{M_y,1}}, \sqrt{a_{M_z,1}}, \sqrt{a_{f,2}}, \sqrt{a_{M_x,2}}, \sqrt{a_{M_y,2}}, \sqrt{a_{M_z,2}})$$

After algebraic manipulation we get:

$$u_c^* = H^{-1}(\Gamma H^{-1})^+ u_s = H^{-2}\Gamma^T(\Gamma H^{-2}\Gamma^T)^{-1}u_s$$

, where $+$ denotes the Moore-Penrose inverse. The control distribution approach is adopted from [27].

2.4 Scenario

When there is a trouble on motor thrust, takeoff is a difficult mission to most multirotor system. Once the multirotor system with motor thrust problem succeeds to take off, the multirotor system usually can achieve some smooth flight trajectory. However, when it comes to flight performance or other estimation applications, the trouble on motor thrust would seriously influence on them. When the above situation occurs, the estimation value and flight performance might be bad. Furthermore, if researchers do the experiment with defective motor to develop new control and estimation technique, it's hard to discover that the problem is actually on the hardware. The situation might wastes the effort put by the researchers who don't know the multirotor is equipped with defective motors, not to mention doing quantitative analysis on the defective hardware. Therefore, this research was conducted, and tried to deal with motor thrust efficiency problem.

2.4.1 A Motor efficiency definition

If a motor is offered the appropriate voltage and current according to motor characteristic curves, and the motor is expected to provide with $10N$ thrust. However, the motor provides only $7N$ thrust due to the damage of the motor. The efficiency of the motor is defined as $e^1 = 70\%$. Similarly, if the motor is offered the appropriate voltage and current according to motor characteristic curves, and the motor is expected to provide $20N$ thrust. The motor would provide only $14N$ thrust.

2.4.2 Assumption

Assume that the hardware components in multirotor system is excellent without damage except for the element related to motor thrust. The following conditions that this research doesn't fix:

Condition 1. One of motors of multirotor is totally broken. This condition is easily to be detected by human vision. By replacing the broken motor with new one, this condition can be easily resolved.

Condition 2. The multirotor system can't take off. The motors efficiency on multirotor system is estimated by UKF. The UKF only models the dynamics of the multirotor system flying in the air.

2.5 Tracking Errors and Estimate Errors

Take the multirotor for example. Given a desired trajectory $x_d \in \mathbb{R}^3$, the position and velocity tracking errors are defined as

$$e_x \triangleq x - x_d, \quad (14)$$

$$e_v \triangleq v - v_d, \quad (15)$$

where $v_d \triangleq \dot{x}_d \in \mathbb{R}^3$ is the desired velocity. To address the rotational dynamics in the subsequent analysis, the attitude error function on $\text{SO}(3)$, the attitude tracking error, and the angular velocity tracking error are defined as

$$\Psi(R, R_d) \triangleq \frac{1}{2} \text{tr} [I - R_d^T R], \quad (16)$$

$$e_R \triangleq \frac{1}{2} (R_d^T R - R^T R_d)^\vee, \quad (17)$$

$$e_\Omega \triangleq \Omega - R^T R_d \Omega_d, \quad (18)$$

where $R_d = [\vec{X}_{B_d}, \vec{Y}_{B_d}, \vec{Z}_{B_d}] \in \text{SO}(3)$ is the desired attitude for the multirotor, and $(\cdot)^\vee : \text{SO}(3) \rightarrow \mathbb{R}^3$ is the vee map. Angular velocity $\Omega_d = (R_d^T \dot{R}_d)^\vee$ can be obtained from the rotational dynamics of the multirotor as described in (3).

2.6 Control Objectives

Take the multirotor for example. The flight controller is designed for the multirotor to track a desired trajectory x_d and desired yaw direction \vec{X}_{B_d} , and endure the thrust and moment loss (D_T, D_M) due to the defective motors. These control objectives are described as

$$\left\{ \begin{array}{l} e_x \\ e_v \\ e_R \\ e_\Omega \end{array} \right. \in UUB \mid D_T \leq \bar{D}_T, \|D_M\| \leq \|\bar{D}_M\|, \quad (19)$$

which means the error e_x, e_v, e_R, e_Ω are uniformly and ultimately bounded (UUB), when $D_T \leq \bar{D}_T$ and $\|D_M\| \leq \|\bar{D}_M\|$ where \bar{D}_T and \bar{D}_M is the upper bound of the thrust disturbance and moment disturbance caused by defective motors.



Chapter 3 Motors Efficiency Estimation

3.1 Unscented Kalman Filte (UKF)

A UKF is evolved from Kalman Filter (KF) and Extended Kalman Filter (EKF) [28], [29], [30]. The aforementioned filters are algorithm that uses a number of measurements observed over time, including noise and other disturbances, and produces estimates of unknown variables. Those filters are designed for different application scenarios. According to the assumption and algorithm of KF, an ordinary KF can only be applied on linear system. In order to estimate state on nonlinear systems by using the KF, one of possible approaches is to linearize the nonlinear system, and this is the reason that the researchers developed EKF. However, although EKF can be applied on nonlinear system, it often has a problem on strongly nonlinear system because the linearization of strongly nonlinear system would cause the poor approximation due to the linearization feature. According to the flaws of the linearization, it's necessary to look for other nonlinear system estimator. Luckily, a nonlinear system estimator, UKF, has been evolved from EKF and ensured the estimation effectiveness by numerous simulation and experiment. The UKF deals with the linearization problem by using a deterministic sample points method. The state distribution is again approximated by a gaussian random variable (GRV), but is now represented using a minimal set of carefully chosen sample points. These sample points completely capture the true mean and covariance of the GRV, and when propagated through the true nonlinear system, captures the posterior mean and covariance accurately to the 3rd order (Taylor series expansion) for any nonlinearity. Known that the dynamics of a multirotor is strongly nonlinear, choosing the UKF as the motors efficiency estimator on this research would be a better choice. Therefore, the estimator of this research are selected to be UKF, and the design details of UKF model are represented later.

Estimation of the state of a discrete-time nonlinear dynamic system

$$x_{k+1} = F(x_k) + n_k \quad (20)$$

$$z_k = H(x_k) + v_k \quad (21)$$

where x_k represent the state of the system and z_k is the measurement of the system. The process noise is n_k and the measurement noise is v_k . The system dynamic model $F(\cdot)$ (predict

model) and $H(\cdot)$ (measurement model) are adjusted according to different application scenarios. The subscript of k denotes the time point k . For more UKF theory details please check on UKF paper.

UKF model section is divided into two parts: The multirotor and the cooperative transportation system. Both UKF models are dedicated to estimate the motors efficiency. By discretizing the nonlinear dynamics of the multirotor and the cooperative transportation system, the predict model and measurement of both models are represented as follows.

3.2 The Multirotor UKF Model

3.2.1 The predict model of the multirotor

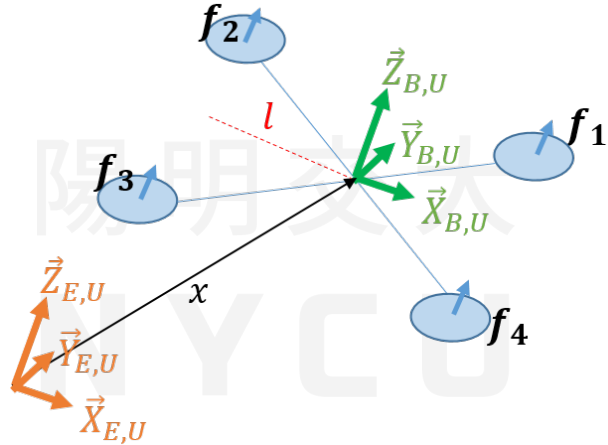


Figure 3: UKF Coordinate systems of four-rotor multirotor

As shown in Fig. 3, the inertial frame and body-fixed frame are defined as $\{ \vec{X}_{E,U}, \vec{Y}_{E,U}, \vec{Z}_{E,U} \}$ and $\{ \vec{X}_{B,U}, \vec{Y}_{B,U}, \vec{Z}_{B,U} \}$ respectively, and the subscript of U means UKF. Comparing Fig. 3 to Fig. 1 , the Fig. 3 is revised the sequence of motors and axis X, Y, Z from North, East, Down (NED) to East, North, Up (ENU). Those changes make the UKF model more intuitive to researchers. In a four-rotor multirotor, the first and third propellers rotate clockwise, and the second and fourth propellers rotate counterclockwise.

UKF Multirotor	Description
$x_k \in \mathbb{R}^3$	multirotor position in the inertial frame
$v_k \in \mathbb{R}^3$	multirotor velocity in the inertial frame
$R_k \in \text{SO}(3)$	rotation matrix from the body-fixed frame to the inertial frame
$\Omega_k \in \mathbb{R}^3$	angular velocity in the body-fixed frame
$f_{d,k} \in \mathbb{R}$	net thrust in the body-fixed frame
$f_{dj,k} \in \mathbb{R}$	thrust generated by the j^{th} propeller
$M_{d,k} \in \mathbb{R}^3$	total moment in the body-fixed frame
$E \in \mathbb{R}^4$	the motors efficiency vector
$e^j \in \mathbb{R}$	efficiency of the j^{th} motor
$m \in \mathbb{R}$	mass
$l \in \mathbb{R}$	the length of motors moment arm
$J \in \mathbb{R}^{3 \times 3}$	inertia matrix
$D_T \in \mathbb{R}^3$	the disturbance of thrust
$D_M \in \mathbb{R}^3$	the disturbance of moment

Table 3: UKF symbol of the multirotor

After discretizing the dynamics from (1) and (3), the predict model is designed as

$$\begin{bmatrix} x_k \\ v_k \\ a_k \\ \Omega_k \\ \alpha_k \\ E_k \end{bmatrix} = \begin{bmatrix} x_{k-1} + v_{k-1}\Delta t + \frac{1}{2}a_{k-1}\Delta t^2 \\ v_{k-1} + a_{k-1}\Delta t \\ \frac{f(E_{k-1})R_{k-1}e_3}{m} - ge_3 \\ \Omega_{k-1} + \alpha_{k-1}\Delta t \\ J^{-1}(M(E_{k-1}) - \Omega_{k-1} \times J\Omega_{k-1}) \\ E_{k-1} \end{bmatrix} \quad (22)$$

where $x_k, v_k, a_k \in \mathbb{R}^3$ represent the position, velocity and acceleration in the inertial frame, respectively, and $f_{d,k} \in \mathbb{R}$ and $M_{d,k} \in \mathbb{R}^3$ are desired thrust and moment control inputs, respectively, in the body-fixed frame. $R_k \in \text{SO}(3)$ is the rotation matrix from the body-fixed frame to the inertial frame, as shown in Fig. 1. m and $g \in \mathbb{R}$ are mass of the multirotor and gravity, respectively, e_3 is an unit vector defined as $e_3 = [0, 0, 1]^T \in \mathbb{R}^3$, $\Omega_k, \alpha_k \in \mathbb{R}^3$ is defined as the angular velocity and angular acceleration of the multirotor, $J \in \mathbb{R}^{3 \times 3}$ is inertia matrix of the multirotor, $E_k \in \mathbb{R}^4$ is the motors efficiency, $\Delta t \in \mathbb{R}$ is sampling time.

The rotational control input $M(E) : \mathbb{R}^4 \rightarrow \mathbb{R}^3$ is defined as $M(E) = \begin{bmatrix} M_x(E) & M_y(E) & M_z(E) \end{bmatrix}^T$. The translational function $f(E) : \mathbb{R}^4 \rightarrow \mathbb{R}$ and $M(E)$ are further defined as

$$\begin{bmatrix} f(E) \\ M_x(E) \\ M_y(E) \\ M_z(E) \end{bmatrix} = \begin{bmatrix} 1 & 1 & 1 & 1 \\ l & l & -l & -l \\ -l & l & l & -l \\ c_{\tau f} & -c_{\tau f} & c_{\tau f} & -c_{\tau f} \end{bmatrix} \begin{bmatrix} e^1 & 0 & 0 & 0 \\ 0 & e^2 & 0 & 0 \\ 0 & 0 & e^3 & 0 \\ 0 & 0 & 0 & e^4 \end{bmatrix} \begin{bmatrix} f_{d1} \\ f_{d2} \\ f_{d3} \\ f_{d4} \end{bmatrix}$$

$$= \Lambda E_{diag} F_d \quad (23)$$

where $\Lambda \in \mathbb{R}^{4 \times 4}$ is a allocation matrix in UKF model, $E_{diag} \in \mathbb{R}^{4 \times 4}$ is a diagonal of the motors efficiency vector $E = [e^1 \ e^2 \ e^3 \ e^4]^T$, e^j is a motor efficiency of the j^{th} motor, $F_d \in \mathbb{R}^4$ is a motor thrusts vector, $l \in \mathbb{R}$ is the length of motors moment arm.

$$\Lambda = \begin{bmatrix} 1 & 1 & 1 & 1 \\ l & l & -l & -l \\ -l & l & l & -l \\ c_{\tau f} & -c_{\tau f} & c_{\tau f} & -c_{\tau f} \end{bmatrix} \quad (24)$$

$$E_{diag} = \begin{bmatrix} e^1 & 0 & 0 & 0 \\ 0 & e^2 & 0 & 0 \\ 0 & 0 & e^3 & 0 \\ 0 & 0 & 0 & e^4 \end{bmatrix} \quad (25)$$

$$F_d = \begin{bmatrix} f_{d1} \\ f_{d2} \\ f_{d3} \\ f_{d4} \end{bmatrix} \quad (26)$$

3.2.2 The measurement model of the multirotor

$$\begin{bmatrix} x_k \\ \Omega_k \end{bmatrix} = \begin{bmatrix} x_k \\ \Omega_k \end{bmatrix} \quad (27)$$

3.3 The cooperative transportation system(CTS) UKF Model

The CTS is rigidly connected by three objects, quadrotor1, quadrotor2 and payload, and they can be abbreviated as q1, q2, p respectively as well as the CTS can be abbreviated as s. The objective of this section is to estimate the motors efficiency of both multirotors in the CTS while the CTS is following a trajectory and transporting a payload. In order to build the nonlinear dynamics model of the cooperative system, it's necessary to clearly define the measurement. At the thought of estimating motors efficiency of both multirotors in the CTS by UKF, it is intuitive that some sensors might be equipped with multirotors and payload. By trying different combinations of dynamics, state and measurement, the objective only needs the position, angular velocity and torque sensors on payload to be achieved.

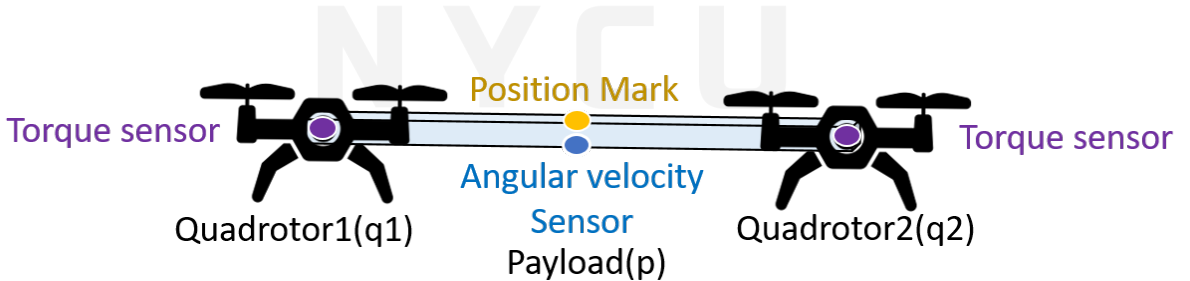


Figure 4: Sensor position of the cooperative transportation system

As shown in Fig. 4, q1, q2 and p represent the quadrotor1, quadrotor2 and payload respectively, and they are rigidly connected. Therefore, their attitude related dynamics are the same. For simplicity, the position of the position mark on the payload is assumed to be the center of mass (COM) of the CTS system.

It's hard to estimate each motor efficiency in the CTS without the force/torque sensor because it's difficult to distinguish the thrust loss are caused by q1 or q2 with only position and angular velocity sensor on the payload. However, the force/torque sensor is quite expensive and it's possible to damage the force/torque sensor during the air crash. Therefore, in order to get

rid of the force/torque sensor, it's important to separate q1, q2, p from the CTS and analyze their independent dynamics for the further model analysis. After trying many different combinations of dynamics and UKF model to estimate the motors efficiency in the CTS, the torque sensor is still needed. However, the translational force sensor can be removed.

3.3.1 The multirotors kinematics related to the CTS system

For the sake of reducing costs, although the CTS UKF measurement model needs the position and angular velocity sensor information of the multirotors, those information could be replaced by the use of sensor information on the payload by using Chasles' theorem. In kinematics, Chasles' theorem has discovered that an ordinary rigid body displacement could be represented by a translation and a followed a rotation [31].

$$\begin{aligned} x_{i/s} &= x_i - x_s \\ a_i &= a_s + \dot{\Omega} \times x_{i/s} + \Omega \times (\Omega \times x_{i/s}) \\ \alpha_i &= \alpha_s \end{aligned} \tag{28}$$

where $x_i, x_s \in \mathbb{R}^3$ represent the multirotors, payload and the CTS position in the inertial frame, respectively, and $x_{i/s} \in \mathbb{R}^3$ is the relative position in the inertial frame, $a_i, a_s \in \mathbb{R}^3$ represent the acceleration of the multirotors and the CTS respectively, $\alpha_i, \alpha_s \in \mathbb{R}^3$ represent angular acceleration of the multirotor and the CTS respectively.

3.3.2 The Physical Specifications of the CTS

For simplicity, the position of the CTS COM is assumed to be overlapped with the position mark on payload. The COM of the CTS is described as

$$x_s = \frac{\sum_i m_i x_i}{\sum_i m_i}, i = 1, 2, p \tag{29}$$

where $m_i \in \mathbb{R}$ can represent the mass of q1, q2 and p.

The mass of the CTS are described as

$$m_s = \sum_i m_i, i = 1, 2, p \quad (30)$$

The moment of inertia of the CTS are described as

$$J_i = \begin{bmatrix} J_{xx,i} & 0 & 0 \\ 0 & J_{yy,i} & 0 \\ 0 & 0 & J_{zz,i} \end{bmatrix} \quad (31)$$

$$\begin{aligned} J_{xx,s} &= \sum_i (J_{xx,i} + m_i(y_i^{S,U^2} + z_i^{S,U^2})) \\ J_{yy,s} &= \sum_i (J_{yy,i} + m_i(x_i^{S,U^2} + z_i^{S,U^2})) \\ J_{zz,s} &= \sum_i (J_{zz,i} + m_i(y_i^{S,U^2} + x_i^{S,U^2})), i = 1, 2, p \end{aligned} \quad (32)$$

where J_i can represent the moment of inertia of q1, q2, p and the CTS.

3.3.3 The dynamics of the independent multirotor in CTS

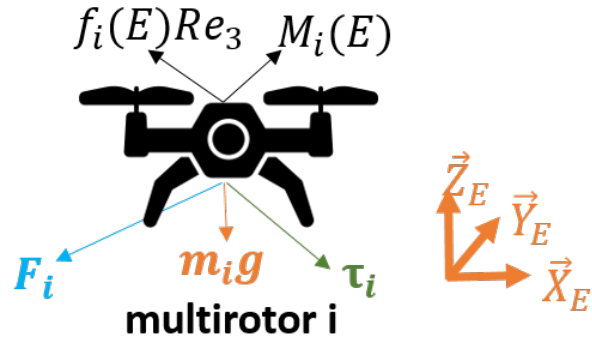


Figure 5: Mechanical analysis of the independent multirotor in CTS

The dynamics of the independent multirotor in CTS is formulated as

$$\dot{x}_i = v_i, \quad (33)$$

$$m_i \dot{v}_i = m_i g e_3 - f_{d,i} R e_3 + F_i, \quad (34)$$

$$\dot{R} = R \hat{\Omega}, \quad (35)$$

$$J_i \dot{\Omega} = M_{d,i} - \Omega \times J \Omega + \tau_i, \quad (36)$$

where i here represents one of q1 and q2, $x_i, v_i \in \mathbb{R}^3$ represent the position and velocity in the inertial frame, respectively, $f_{d,i} \in \mathbb{R}$ and $M_{d,i} \in \mathbb{R}^3$ are desired thrust and moment control inputs, respectively, in the body-fixed frame, $F_i \in \mathbb{R}^3$ is the external force exerted by the payload, $\tau_i \in \mathbb{R}^3$ is the external torque exerted by the payload, $R \in SO(3)$ is the rotation matrix from the body-fixed frame to the inertial frame, as shown in Fig. 5. m and $g \in \mathbb{R}$ are mass of the multirotor and gravity, respectively, e_3 is an unit vector defined as $e_3 = [0, 0, 1]^T \in \mathbb{R}^3$, $\Omega \in \mathbb{R}^3$ is defined as the angular velocity, $\dot{\Omega} \in \mathbb{R}^3$ is the angular acceleration, $J_i \in \mathbb{R}^{3 \times 3}$ is inertia matrix.

3.3.4 The dynamics of the independent payload in CTS

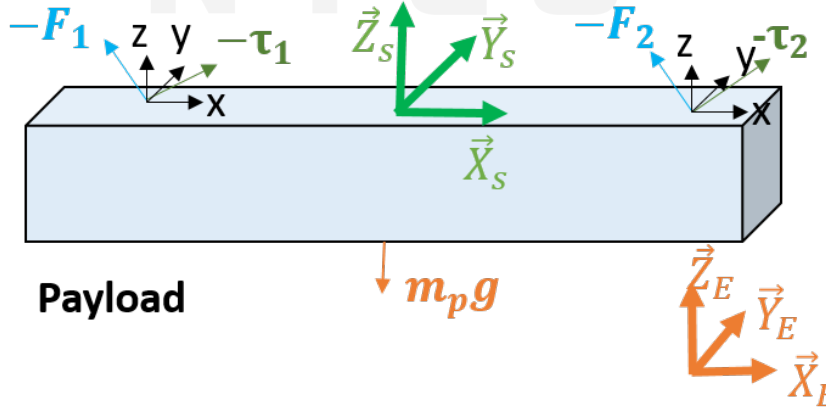


Figure 6: Mechanical analysis of the independent payload in CTS

The dynamics of the independent payload in CTS is formulated as

$$\dot{x}_p = v_p, \quad (37)$$

$$m_p \dot{v}_p = -(F_1 + F_2) - m_p g e_3, \quad (38)$$

$$\dot{R} = R \hat{\Omega}, \quad (39)$$

$$J_p \dot{\Omega} = -(\tau_1 + \tau_2) + M_p(F_1, F_2) - \Omega \times J_p \Omega, \quad (40)$$

where $M_p(F_1, F_2) : \mathbb{R}^3 \times \mathbb{R}^3 \rightarrow \mathbb{R}^3$ is the function represents the torque caused from the multirotors translational force exerts on the payload, and it is defined as

$$M_p(F_1, F_2) = \begin{bmatrix} 0 & 0 & 0 \\ 0 & 0 & 0.5 \\ 0 & -0.5 & 0 \end{bmatrix} (-F_1^s) + \begin{bmatrix} 0 & 0 & 0 \\ 0 & 0 & -0.5 \\ 0 & 0.5 & 0 \end{bmatrix} (-F_2^s) \quad (41)$$

where $-F_1^s, -F_2^s$ is the force exerted by the q1 and q2 in the CTS body-fixed frame respectively, $-F_1$ and $-F_2$ are the force exerted by q1 and q2 in the inertial frame respectively, $-\tau_1$ and $-\tau_2$ are the torque exerted by q1 and q2 in the body-fixed frame respectively, $x_p, v_p \in \mathbb{R}^3$ represent the position and velocity in the inertial frame, respectively, $R \in SO(3)$ is the rotation matrix from the body-fixed frame to the inertial frame, as shown in Fig. 6. m and $g \in \mathbb{R}$ are mass of the multirotor and gravity, respectively, e_3 is an unit vector defined as $e_3 = [0, 0, 1]^T \in \mathbb{R}^3$, $\Omega \in \mathbb{R}^3$ is defined as the angular velocity, $\dot{\Omega} \in \mathbb{R}^3$ is the angular acceleration, $J_p \in \mathbb{R}^{3 \times 3}$ is inertia matrix.

3.3.5 The predict model of the CTS

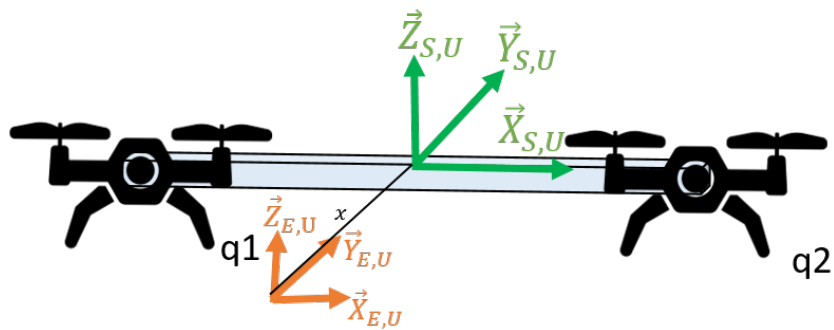


Figure 7: UKF Coordinate systems of the cooperative transportation system

As shown in Fig. 7, the inertial frame and body-fixed frame are defined as $\{ \vec{X}_{E,U}, \vec{Y}_{E,U}, \vec{Z}_{E,U} \}$ and $\{ \vec{X}_{S,U}, \vec{Y}_{S,U}, \vec{Z}_{S,U} \}$ respectively, and the subscript of s means system. Comparing Fig. 2 to Fig. 7, the Fig. 7 is revised the sequence of motors and axis X, Y, Z from North, East, Down (NED) to East, North, Up (ENU).

CTS Symbol	Description
i	the subscript i , which represents one of quadrotor1(q1),quadrotor2(q2),payload(p)
j	the subscript j , which represents one of 1,2,3,4
$x_{i,k} \in \mathbb{R}^3$	position of i in the inertial frame
$v_{i,k} \in \mathbb{R}^3$	velocity of i in the inertial frame
$a_{i,k} \in \mathbb{R}^3$	acceleration of i in the inertial frame
$R_k \in \text{SO}(3)$	rotation matrix from the body-fixed frame to the inertial frame
$\Omega_k \in \mathbb{R}^3$	angular velocity in the body-fixed frame
$\alpha_k \in \mathbb{R}^3$	angular acceleration in the body-fixed frame
$E_{i,k} \in \mathbb{R}^4$	motors efficiency vector of i
$e_i^j \in \mathbb{R}$	efficiency value of i multirotor and j^{th} motor
$f_{d,s,k} \in \mathbb{R}$	net thrust of the CTS in the body-fixed frame
$f_{dj,i} \in \mathbb{R}$	distributed thrust generated by the j^{th} propeller of the i^{th} multirotor
$M_{d,s,k} \in \mathbb{R}^3$	total moment of the CTS in the body-fixed frame
$m_s \in \mathbb{R}$	mass of the CTS
$J_s \in \mathbb{R}^{3 \times 3}$	inertia matrix of the CTS

Table 4: UKF symbol of the cooperative transportation system

After discretizing the dynamics from 34, 38, 36, 40, the predict model is designed as

$$\begin{bmatrix} x_{1,k} \\ v_{1,k} \\ a_{1,k} \\ \Omega_{1,k} \\ \alpha_{1,k} \\ E_{1,k} \\ x_{2,k} \\ v_{2,k} \\ a_{2,k} \\ \Omega_{2,k} \\ \alpha_{2,k} \\ E_{2,k} \\ x_{p,k} \\ v_{p,k} \\ a_{p,k} \\ \Omega_{p,k} \\ \alpha_{p,k} \\ F_{1,k} \\ F_{2,k} \end{bmatrix} = \begin{bmatrix} x_{1,k-1} + v_{1,k-1}\Delta t + \frac{1}{2}\alpha_{1,k-1}\Delta t^2 \\ v_{1,k-1} + a_{1,k-1}\Delta t \\ \frac{f_1(E_{1,k-1})R_{k-1}e_3}{m_1} - ge_3 + \frac{F_{1,k-1}}{m_1} \\ \Omega_{1,k-1} + \alpha_{1,k-1}\Delta t \\ \alpha_{1,k-1} \\ E_{1,k-1} \\ x_{2,k-1} + v_{2,k-1}\Delta t + \frac{1}{2}\alpha_{2,k-1}\Delta t^2 \\ v_{2,k-1} + a_{2,k-1}\Delta t \\ \frac{f_2(E_{2,k-1})R_{k-1}e_3}{m_2} - ge_3 + \frac{F_{2,k-1}}{m_2} \\ \Omega_{2,k-1} + \alpha_{2,k-1}\Delta t \\ \alpha_{2,k-1} \\ E_{2,k-1} \\ x_{p,k-1} + v_{p,k-1}\Delta t + \frac{1}{2}\alpha_{p,k-1}\Delta t^2 \\ v_{p,k-1} + a_{p,k-1}\Delta t \\ \frac{-(F_1+F_2)}{m_p} - ge_3 \\ \Omega_{p,k-1} + \alpha_{p,k-1}\Delta t \\ J_p^{-1}[M_p(F_1, F_2) - (\tau_{1,k} + \tau_{2,k}) - \Omega_{p,k} \times J_p \Omega_{p,k}] \\ F_{1,k-1} \\ F_{2,k-1} \end{bmatrix} \quad (42)$$

where $x_{1,k}, x_{2,k}, x_{p,k} \in \mathbb{R}^3$ represent the position of q1, q2, p in the inertial frame respectively, and $v_{1,k}, v_{2,k}, v_{p,k} \in \mathbb{R}^3$ represent the velocity of q1, q2, p in the inertial frame respectively, $a_{1,k}, a_{2,k}, a_{p,k} \in \mathbb{R}^3$ represent the acceleration of q1, q2, p in the inertial frame respectively, $\Omega_{1,k}, \Omega_{2,k}, \Omega_{p,k} \in \mathbb{R}^3$ the angular velocity of q1, q2, p in the body-fixed frame respectively $\alpha_{1,k}, \alpha_{2,k}, \alpha_{p,k} \in \mathbb{R}^3$ the angular acceleration of q1, q2, p in the body-fixed frame respectively, $E_{1,k}, E_{2,k} \in \mathbb{R}^4$ are the motors efficiency of q1, q2 respectively, $F_{1,k}, F_{2,k} \in \mathbb{R}^3$ are the force exerted from p to q1, q2 in the inertial frame respectively, $R_k \in \text{SO}(3)$ is the rotation matrix from the body-fixed frame to the inertial frame, the function $f_1(E_1)$ and $f_2(E_2)$ can be obtained from (23).

3.3.6 The measurement model of the CTS

$$\begin{bmatrix} x_{1,k} \\ \Omega_{1,k} \\ \tau_{1,k} \\ x_{2,k} \\ \Omega_{2,k} \\ \tau_{2,k} \\ x_{p,k} \\ \Omega_{p,k} \end{bmatrix} = \begin{bmatrix} x_{1,k} \\ \Omega_{1,k} \\ J_1\alpha_{1,k} - (M_1(E_{1,k}) - \Omega_k \times J_1\Omega_k) \\ x_{2,k} \\ \Omega_{2,k} \\ J_2\alpha_{2,k} - (M_2(E_{2,k}) - \Omega_k \times J_2\Omega_k) \\ x_{p,k} \\ \Omega_{p,k} \end{bmatrix} \quad (43)$$

where $\tau_{1,k}, \tau_{2,k} \in \mathbb{R}^3$ represent the torque exerted from payload to q1, q2 in the body-fixed frame respectively, the function $M_1(E_1)$ and $M_2(E_2)$ can be obtained from (23).

3.4 UKF Observability

x represents a state vector in this section and $z(x)$ is a measurement vector in (20) and (21), [32], [33].

$$O \triangleq \frac{\partial \phi}{\partial x} = \begin{bmatrix} \frac{\partial \mathcal{L}_f^0(z(x))}{\partial x_1} & \dots & \frac{\partial \mathcal{L}_f^0(z(x))}{\partial x_n} \\ \vdots & \ddots & \vdots \\ \frac{\partial \mathcal{L}_f^{n-1}(z(x))}{\partial x_1} & \dots & \frac{\partial \mathcal{L}_f^{n-1}(z(x))}{\partial x_n} \end{bmatrix} \quad (44)$$

where O is an observability matrix, and the dimension of O depends on the derivative times. The elements of state x are x_1, x_2, \dots, x_n . ϕ is defined as

$$\phi \triangleq \begin{bmatrix} \mathcal{L}_f^0(z(x)) \\ \mathcal{L}_f^1(z(x)) \\ \vdots \\ \mathcal{L}_f^{n-1}(z(x)) \end{bmatrix} \quad (45)$$

The elements are defined as

$$\begin{aligned}
\mathcal{L}_f^0(z(x)) &\triangleq z(x) \\
\mathcal{L}_f^1(z(x)) &\triangleq \frac{\partial z(x)}{\partial x} \cdot f \\
\mathcal{L}_f^2(z(x)) &\triangleq \frac{\partial}{\partial x} \left[\mathcal{L}_f^1(z(x)) \right] \cdot f \\
&\vdots \\
\mathcal{L}_f^k(z(x)) &\triangleq \frac{\partial}{\partial x} \left[\mathcal{L}_f^{k-1}(z(x)) \right] \cdot f
\end{aligned} \tag{46}$$

where $f = \dot{x}$. If $\text{rank}(O)$ is full rank, the system is observable.

The observability matrix dimension of the multirotor and the CTS are too big to be analyzed by human. Therefore, the subsequent analysis is conducted by Matlab. The source code is put at the url https://github.com/ChangChiaChengcccc/UKF_Observability-Analysis. Matlab offers symbolic math toolbox, the variables in Matlab can be treated as symbols. The symbols can be manipulated as functions, and the functions can be further computed. The toolbox provides functions in common mathematical areas such as calculus, linear algebra, algebraic and differential equations, equation simplification, and equation manipulation.

Chapter 4 Controller Design

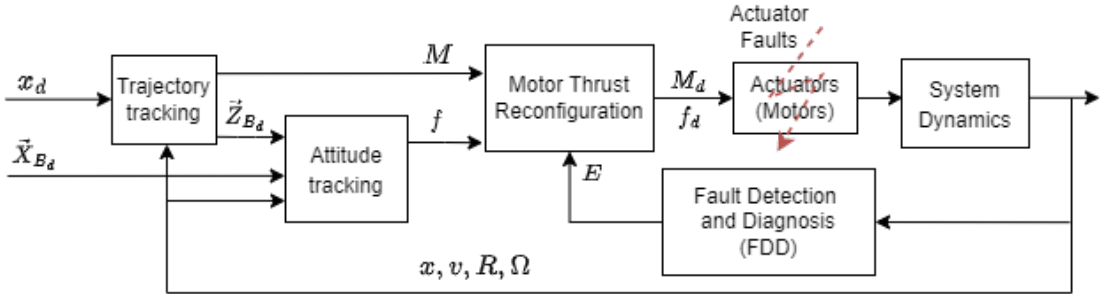


Figure 8: Control Flow

This controller is suitable to rigidly connected system, so it can be applied on both the multirotor and the cooperative transportation system. For concisely introducing controller design, chapters of Controller Design and Stability Analysis would take the multirotor as an example, and omit the CTS. To achieve the aforementioned control objectives of the multirotor as well as endure the thrust and the moment disturbance (D_T, D_M) due to the defective motors and the feedback estimation error of motors efficiency. The feedback estimation of motors efficiency adjusts ordinary control input from f, M to f_d, M_d , which is clearly described in Fig. 9 and Sec. 4.3. Translational and rotational controllers f and M are designed based on geometric tracking controller, as described below.

4.1 Translational Controller for the Multirotor

Let the translational controller be designed as

$$f = ((k_x + k_{xD})e_x + (k_v + k_{vD})e_v + mge_3 - m\ddot{x}_d) \cdot Re_3 \quad (47)$$

where k_x, k_{xD}, k_v, k_{vD} are positive control gains, and k_{xD}, k_{vD} are designed to deal with the disturbance D_T .

Note that the controller designed in (47) is the net thrust obtained by projecting the force control input \vec{f} into e_3 on the body frame:

$$\vec{f} = (k_x + k_{xD})e_x + (k_v + k_{vD})e_v + mge_3 - m\ddot{x}_d \quad (48)$$

4.2 Rotational Controller for the Multicopter

The subsequent analysis is facilitated by making the following assumption:

$$\|((k_x + k_{xD})e_x + (k_v + k_{vD})e_v + mge_3 - m\ddot{x}_d)\| \neq 0, \quad (49)$$

and the commanded acceleration is uniformly bounded such that

$$\|-mge_3 + m\ddot{x}_d\| < B$$

where $B \in R_{>0}$ is a positive constant, which are similar to [34].

Let the rotational controller be designed as

$$M = -(k_R + k_{RD})e_R - (k_\Omega + k_{\Omega D})e_\Omega + \Omega \times J\Omega - J\bar{\Omega} \quad (50)$$

where $k_R, k_{RD}, k_\Omega, k_{\Omega D}$ are positive control gains, $k_{RD}, k_{\Omega D}$ are designed to deal with the disturbance D_M , and $\bar{\Omega} \in \mathbb{R}^3$ is defined as

$$\bar{\Omega} = \begin{bmatrix} \bar{\Omega}_1 \\ \bar{\Omega}_2 \\ \bar{\Omega}_3 \end{bmatrix} = \hat{\Omega}R^T R_d \Omega_d - R^T R_d \dot{\Omega}_d \quad (51)$$

where $R_d = \begin{bmatrix} \vec{X}_{B_d} & \vec{Y}_{B_d} & \vec{Z}_{B_d} \end{bmatrix} \in SO(3)$ and

$$\vec{Z}_{B_d} = -\frac{-((k_x + k_{xD})e_x + (k_v + k_{vD})e_v + mge_3 - m\ddot{x}_d)}{\|((k_x + k_{xD})e_x + (k_v + k_{vD})e_v + mge_3 - m\ddot{x}_d)\|} \quad (52)$$

designed using an approach similar to that adopted in [34], are the desired attitude and the z-axis of the body-fixed frame of the multicopter, respectively, and \vec{Z}_{B_d} exists based on (49).

4.3 Reconfiguration with Feedback Motor Efficiency

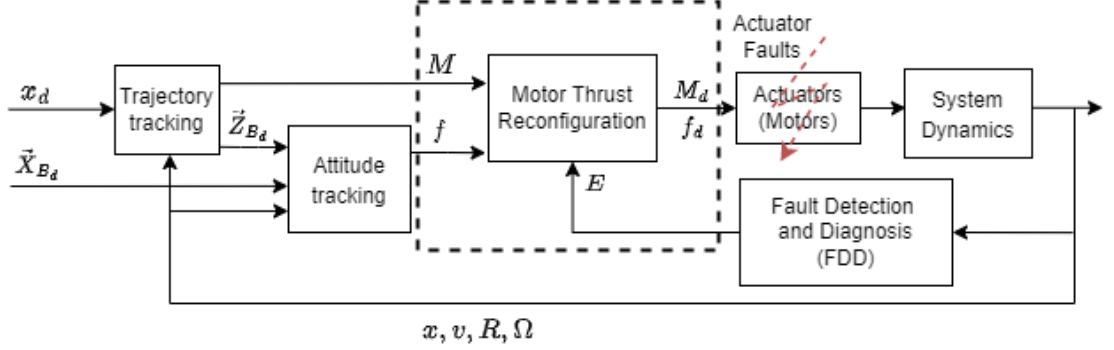


Figure 9: Feedback Efficiency Control Flow

To explain the way to reconfiguration, please look at the area bounded by dotted line rectangle in Fig. 9. With the question 5, the input of the dotted line rectangle can be distributed to $\begin{bmatrix} f_1 & f_2 & f_3 & f_4 \end{bmatrix}^T$ by multiplying the inverse allocation matrix as

$$\begin{bmatrix} f_1 \\ f_2 \\ f_3 \\ f_4 \end{bmatrix} = \begin{bmatrix} 1 & 1 & 1 & 1 \\ 0 & -d & 0 & d \\ d & 0 & -d & 0 \\ -c_{\tau f} & c_{\tau f} & -c_{\tau f} & c_{\tau f} \end{bmatrix}^{-1} \begin{bmatrix} f \\ M_x \\ M_y \\ M_z \end{bmatrix} \quad (53)$$

Next, the feedback efficiency E reconfigures $\begin{bmatrix} f_1 & f_2 & f_3 & f_4 \end{bmatrix}^T$ as

$$\begin{bmatrix} f_{d1} \\ f_{d2} \\ f_{d3} \\ f_{d4} \end{bmatrix} = \begin{bmatrix} \frac{1}{e^1} & 0 & 0 & 0 \\ 0 & \frac{1}{e^2} & 0 & 0 \\ 0 & 0 & \frac{1}{e^3} & 0 \\ 0 & 0 & 0 & \frac{1}{e^4} \end{bmatrix} \begin{bmatrix} f_1 \\ f_2 \\ f_3 \\ f_4 \end{bmatrix} \quad (54)$$

where $e^j \in \mathbb{R}$ is the j^{th} motor efficiency. $\begin{bmatrix} f_{d1} & f_{d2} & f_{d3} & f_{d4} \end{bmatrix}^T$ can be represented for the control input after reconfiguration with the allocation matrix as

$$\begin{bmatrix} f_d \\ M_d \end{bmatrix} = \begin{bmatrix} 1 & 1 & 1 & 1 \\ 0 & -d & 0 & d \\ d & 0 & -d & 0 \\ -c_{\tau f} & c_{\tau f} & -c_{\tau f} & c_{\tau f} \end{bmatrix} \begin{bmatrix} f_{d1} \\ f_{d2} \\ f_{d3} \\ f_{d4} \end{bmatrix} \quad (55)$$

where $f_d \in \mathbb{R}$ is the net thrust after reconfiguration, $M_d \in \mathbb{R}^3$ is the moment of inertia after reconfiguration.

4.4 Closed-Loop Error System

To facilitate the stability analysis presented in Chapter 5, the closed-loop error systems of rotational and translational dynamics are derived in this section.

4.4.1 Translational Dynamics

Taking the time derivative of (15) and substituting the translational dynamics of the multirotor defined in (2) yields

$$\begin{aligned} m\dot{e}_v &= m\ddot{x} - m\ddot{x}_d \\ &= mge_3 - fRe_3 + D_T Re_3 - m\ddot{x}_d \\ &= mge_3 - m\ddot{x}_d + D_T Re_3 - \frac{f}{e_3^T R_d^T Re_3} \cdot R_d e_3 - X \end{aligned} \quad (56)$$

where $X \in \mathbb{R}^3$ is defined as

$$X = \frac{f}{e_3^T R_d^T Re_3} ((e_3^T R_d^T Re_3) Re_3 - R_d e_3)$$

Afterwards, substituting with f with (47) yields

$$m\dot{e}_v = -(k_x + k_{xD})e_x - (k_v + k_{vD})e_v - X + D_T Re_3 \quad (57)$$

4.4.2 Rotational Dynamics

Taking the time derivative of error dynamics e_R and e_Ω defined in (17) and (18) yields

$$\begin{aligned}\dot{e}_R &= \frac{1}{2}(R_d^T R \hat{e}_\Omega + \hat{e}_\Omega R^T R_d)^\vee \\ &= C(R_d^T R)e_\Omega,\end{aligned}\tag{58}$$

$$\begin{aligned}\dot{e}_\Omega &= \dot{\Omega} + (\hat{\Omega} R^T R_d \Omega_d - R^T R_d \dot{\Omega}_d) \\ &= \dot{\Omega} + \bar{\Omega},\end{aligned}\tag{59}$$

where $C(R_d^T R)$ is defined as

$$C(R_d^T R) \triangleq \frac{1}{2}(\text{tr}[R^T R_d]I - R^T R_d).\tag{60}$$

Multiplying (59) by J and substituting the rotation dynamics of the multirotor (4) into (59) yields

$$\begin{aligned}J\dot{e}_\Omega &= J\dot{\Omega} + J\bar{\Omega} \\ &= M - \Omega \times J\Omega - D_M + J\bar{\Omega}\end{aligned}\tag{61}$$

Afterwards, substituting with M with (50) yields

$$J\dot{e}_\Omega = -(k_R + k_{RD})e_R - (k_\Omega + k_{\Omega D})e_\Omega - D_M$$

Chapter 5 Stability Analysis

The stability analysis of this controller can be divided into two parts: rotational and translational. Lyapunov functions V_1 and V_2 are designed to prove the stability of the translational and rotational dynamics, respectively. The stability of the overall system is then proven by using $V = V_1 + V_2$ [35].

5.1 Stability Analysis of the Rotational Dynamics

Theorem 1. *The controller designed in (50) can ensure e_R and e_Ω are bounded and $\Psi(R(t), R_d(t))$ and ψ_2 defined in (16) and (70) satisfy*

$$\Psi(R(t), R_d(t)) \leq \psi_2 < 2 \quad (62)$$

provided that the following conditions are satisfied

$$\Psi(R(0), R_d(0)) < 2 \quad (63)$$

$$\|e_\Omega(0)\| < \frac{2}{\lambda_{\max}(J)}(k_R + k_{RD})(2 - \Psi(R(0), R_d(0))) \quad (64)$$

$$c_2 < \min\{(k_\Omega + k_{\Omega D}),$$

$$\left. \frac{4(k_\Omega + k_{\Omega D})(k_R + k_{RD})\lambda_{\min}(J)^2}{(k_\Omega + k_{\Omega D})^2\lambda_{\max}(J) + 4(k_\Omega + k_{\Omega D})(k_R + k_{RD})\lambda_{\min}(J)^2}, \sqrt{(k_R + k_{RD})\lambda_{\min}(J)} \right\} \quad (65)$$

where c_2 is a positive constant.

Proof. Let V_2 be defined as

$$V_2 = \frac{1}{2}e_\Omega \cdot Je_\Omega + (k_R + k_{RD})\Psi(R, R_d) + c_2 e_R \cdot e_\Omega \quad (66)$$

which can be lower and upper bounded by

$$z_2^T M_{21} z_2 \leq V_2 \leq z_2^T M_{22} z_2, \quad (67)$$

where $z_2 \triangleq \begin{bmatrix} \|e_R\|, & \|e_\Omega\| \end{bmatrix}^T$

$$M_{21} = \frac{1}{2} \begin{bmatrix} k_R + k_{RD} & -c_2 \\ -c_2 & \lambda_{min}(J) \end{bmatrix}, \quad (68)$$

$$M_{22} = \frac{1}{2} \begin{bmatrix} \frac{2(k_R + k_{RD})}{2 - \psi_2} & c_2 \\ c_2 & \lambda_{max}(J) \end{bmatrix}, \quad (69)$$

where $\psi_2 \in \mathbb{R}$ is defined as

$$\psi_2 = \frac{1}{k_R + k_{RD}} \left[\frac{1}{2} e_\Omega(0) \cdot J e_\Omega(0) + (k_R + k_{RD}) \Psi(R(0), R_d(0)) \right]. \quad (70)$$

Taking the time derivative of V_2 yields

$$\dot{V}_2 = e_\Omega \cdot J \dot{e}_\Omega + (k_R + k_{RD}) \frac{d}{dt} (\Psi(R, R_d)) + c_2 \dot{e}_R \cdot e_\Omega + c_2 e_R \cdot \dot{e}_\Omega \quad (71)$$

the second term $\frac{d}{dt} (\Psi(R, R_d))$ can be written as

$$\begin{aligned}
\frac{d}{dt}(\Psi(R, R_d)) &= \frac{d}{dt} \left(\frac{1}{2} \text{tr} [I - R_d^T R] \right) \\
&= \frac{1}{2} \text{tr} \left[-\dot{R}_d^T R - R_d^T \dot{R} \right] \\
&= -\frac{1}{2} \text{tr} \left[R_d^T \hat{\Omega}_d^T R + R_d^T R \hat{\Omega} \right] \\
&= -\frac{1}{2} \text{tr} \left[R_d^T R \hat{\Omega} - R_d^T R R^T R_d \hat{\Omega}_d R_d^T R \right] \\
&= -\frac{1}{2} \text{tr} \left[R_d^T R (\Omega - R^T R_d \Omega_d)^\wedge \right] \\
&= -\frac{1}{2} \text{tr} \left[R_d^T R \hat{e}_\Omega \right] \\
&= -\frac{1}{2} \left(\frac{1}{2} \text{tr} [R_d^T R \hat{e}_\Omega - \hat{e}_\Omega R^T R_d] \right) \\
&= -\frac{1}{2} (\text{tr} [\hat{e}_\Omega \hat{e}_R]) \\
&= e_\Omega \cdot e_R
\end{aligned}$$

Substitute $\frac{d}{dt}(\Psi(R, R_d))$, \dot{e}_Ω and \dot{e}_R into \dot{V}_2

$$\begin{aligned}
\dot{V}_2 &= e_\Omega \cdot J \dot{e}_\Omega + (k_R + k_{RD}) \frac{d}{dt}(\Psi(R, R_d)) + c_2 \dot{e}_R \cdot e_\Omega + c_2 e_R \cdot \dot{e}_\Omega \\
&= e_\Omega \cdot J \dot{e}_\Omega + (k_R + k_{RD}) e_R \cdot e_\Omega + c_2 \dot{e}_R \cdot e_\Omega + c_2 e_R \cdot \dot{e}_\Omega \\
&= e_\Omega \cdot (-(k_R + k_{RD}) e_R - (k_\Omega + k_{\Omega D}) e_\Omega - D_M) + (k_R + k_{RD}) e_R \cdot e_\Omega + c_2 \dot{e}_R \cdot e_\Omega \\
&\quad + c_2 e_R \cdot J^{-1}(-(k_R + k_{RD}) e_R - (k_\Omega + k_{\Omega D}) e_\Omega - D_M) \\
&= -k_\Omega \|e_\Omega\|^2 - c_2 k_R e_R \cdot J^{-1} e_R + c_2 C(R_d^T R) e_\Omega \cdot e_\Omega - c_2 (k_\Omega + k_{\Omega D}) e_R \cdot J^{-1} e_\Omega \\
&\quad - k_{\Omega D} \|e_\Omega\|^2 - c_2 k_{RD} e_R \cdot J^{-1} e_R - e_\Omega \cdot D_M - c_2 e_R \cdot J^{-1} D_M \tag{72}
\end{aligned}$$

Since $C(R_d^T R)$ defined in (60) can be bounded as $\|C(R_d^T R)\| \leq 1$, substituting into (72) yields

$$\begin{aligned}
\dot{V}_2 &\leq -(k_\Omega - c_2) \|e_\Omega\|^2 - \frac{c_2 k_R}{\lambda_{\max}(J)} \|e_R\|^2 + \frac{c_2 (k_\Omega + k_{\Omega D})}{\lambda_{\min}(J)} \|e_R\| \|e_\Omega\| \\
&\quad - k_{\Omega D} \|e_\Omega\|^2 - \frac{c_2 k_{RD}}{\lambda_{\max}(J)} \|e_R\|^2 + \bar{D}_M \|e_\Omega\| + \frac{c_2 \bar{D}_M}{\lambda_{\min}(J)} \|e_R\|
\end{aligned}$$

By the method of completing the square, we know that

$$-ax^2 + bx = -a(x - \frac{b}{2a})^2 + \frac{b^2}{4a}$$

and

$$\begin{aligned} -k_{\Omega D}\|e_{\Omega}\|^2 + \bar{D}_M\|e_{\Omega}\| &= -k_{\Omega D}(\|e_{\Omega}\| - \frac{\bar{D}_M}{2k_{\Omega D}})^2 + \frac{\bar{D}_M^2}{4k_{\Omega D}} \\ -\frac{c_2 k_{RD}}{\lambda_{max}(J)}\|e_R\|^2 + \frac{c_2 \bar{D}_M}{\lambda_{min}(J)}\|e_R\| &= -\frac{c_2 k_{RD}}{\lambda_{max}(J)}(\|e_R\| - \frac{\bar{D}_M \lambda_{max}(J)}{2k_{RD} \lambda_{min}(J)})^2 + \frac{c_2 \bar{D}_M^2 \lambda_{max}(J)}{4k_{RD} \lambda_{min}^2(J)} \end{aligned}$$

substituting into \dot{V}_2 yields

$$\begin{aligned} \dot{V}_2 &\leq -(k_{\Omega} - c_2)\|e_{\Omega}\|^2 - \frac{c_2 k_R}{\lambda_{max}(J)}\|e_R\|^2 + \frac{c_2(k_{\Omega} + k_{\Omega D})}{\lambda_{min}(J)}\|e_R\|\|e_{\Omega}\| \\ &\quad - k_{\Omega D}(\|e_{\Omega}\| - \frac{\bar{D}_M}{2k_{\Omega D}})^2 + \frac{\bar{D}_M^2}{4k_{\Omega D}} - \frac{c_2 k_{RD}}{\lambda_{max}(J)}(\|e_R\| - \frac{\bar{D}_M \lambda_{max}(J)}{2k_{RD} \lambda_{min}(J)})^2 + \frac{c_2 \bar{D}_M^2 \lambda_{max}(J)}{4k_{RD} \lambda_{min}^2(J)} \\ &\leq - \begin{bmatrix} \|e_R\| & \|e_{\Omega}\| \end{bmatrix} \begin{bmatrix} \frac{c_2 k_R}{\lambda_{max}(J)} & -\frac{c_2(k_{\Omega} + k_{\Omega D})}{2\lambda_{min}(J)} \\ -\frac{c_2(k_{\Omega} + k_{\Omega D})}{2\lambda_{min}(J)} & k_{\Omega} - c_2 \end{bmatrix} \begin{bmatrix} \|e_R\| \\ \|e_{\Omega}\| \end{bmatrix} + \frac{\bar{D}_M^2}{4k_{\Omega D}} + \frac{c_2 \bar{D}_M^2 \lambda_{max}(J)}{4k_{RD} \lambda_{min}^2(J)} \\ &\leq -z_2^T W_2 z_2 + \frac{\bar{D}_M^2}{4k_{\Omega D}} + \frac{c_2 \bar{D}_M^2 \lambda_{max}(J)}{4k_{RD} \lambda_{min}^2(J)} \end{aligned} \tag{73}$$

where W_2 is defined as

$$W_2 = \begin{bmatrix} \frac{c_2 k_R}{\lambda_{max}(J)} & -\frac{c_2(k_{\Omega} + k_{\Omega D})}{2\lambda_{min}(J)} \\ -\frac{c_2(k_{\Omega} + k_{\Omega D})}{2\lambda_{min}(J)} & k_{\Omega} - c_2 \end{bmatrix}. \tag{74}$$

With the calculation above, \dot{V}_2 is bounded as

$$\dot{V}_2 \leq -z_2^T W_2 z_2 + \frac{\bar{D}_M^2}{4k_{\Omega D}} + \frac{c_2 \bar{D}_M^2 \lambda_{max}(J)}{4k_{RD} \lambda_{min}^2(J)} \tag{75}$$

To facilitate the subsequent analysis, the analysis is divided into two steps.

Step 1: to prove (62). Supposing that $c_2 = 0$, e_R will drop from (66), and (66) and (75)

can be rewritten as

$$V_2|_{c_2=0} = \frac{1}{2}e_\Omega \cdot Je_\Omega + (k_R + k_{RD})\Psi(R, R_d),$$

$$\dot{V}_2|_{c_2=0} \leq -k_\Omega \|e_\Omega\|^2 + \frac{\bar{D}_M^2}{4k_{\Omega D}},$$

which implies that $V_2|_{c_2=0}$ with a suitable k_Ω is nonincreasing. Therefore, given the initial conditions (63) and (64), the attitude error function can be bounded as

$$(k_R + k_{RD})\Psi(R(t), R_d(t)) \leq V_2|_{c_2=0}(t) \leq V_2|_{c_2=0}(0) < 2(k_R + k_{RD}), \quad (76)$$

which guarantees that

$$\Psi(R(t), R_d(t)) \leq \psi_2 < 2,$$

which proves (62) and ensures the element $\frac{2(k_R + k_{RD})}{2 - \psi_2}$ defined in (69) is positive. Therefore, $R(t)$ always lies in the sublevel set $L_2 \triangleq \{R \in \text{SO}(3) \mid \Psi(R, R_d) < 2\}$. Within sublevel set L_2 , the attitude error function is positive definite:

$$\frac{1}{2}\|e_R\|^2 \leq \Psi \leq \frac{1}{2 - \psi_2}\|e_R\|^2.$$

Step 2: To prove e_R and e_Ω achieve are bounded, the matrices M_{21} , M_{22} , and W_2 defined in (68), (69), and (74) are positive definite by selecting c_2 to satisfy (65). Since V_2 is positive definite and \dot{V}_2 can be adjusted by the disturbance gain $k_{\Omega D}$, k_{RD} based on (67) and (74), Theorem 1 is proven. \square

5.2 Stability Analysis of the Translational Dynamics

To facilitate the subsequent analysis, the following proposition is developed.

Proposition 1. ψ_1 defined in (80) satisfies

$$\Psi(R(t), R_d(t)) \leq \psi_1 < 1. \quad (77)$$

provided that the initial conditions are satisfied

$$\Psi(R(0), R_d(0)) < 1, \quad (78)$$

$$\|e_\Omega(0)\|^2 < \frac{2}{\lambda_{\max}(J)}(k_R + k_{RD})(\psi_1 - \Psi(R(0), R_d(0))), \quad (79)$$

where ψ_1 is defined as

$$\psi_1 = \frac{1}{k_R + k_{RD}} \left[\frac{1}{2} e_\Omega(0) \cdot J e_\Omega(0) + (k_R + k_{RD}) \Psi(R(0), R_d(0)) \right]. \quad (80)$$

Proof. Given the initial conditions (78) and (79), (76) can be written as

$$(k_R + k_{RD})\Psi(R(t), R_d(t)) \leq V_2|_{c_2=0}(t) \leq V_2|_{c_2=0}(0) < (k_R + k_{RD})\psi_1,$$

which guarantees (77). \square

In the translational dynamics, Lyapunov function V_1 containing the position and velocity errors is defined as

$$V_1 = \frac{1}{2}(k_x + k_{xD})e_x \cdot e_x + \frac{1}{2}m e_v \cdot e_v + c_1 e_x \cdot e_v, \quad (81)$$

which can be lower and upper bounded by

$$z_1^T M_{11} z_1 \leq V_1 \leq z_1^T M_{12} z_1$$

where $z_1 = [\|e_x\|, \|e_v\|]^T$, and M_{11} and M_{12} are defined as

$$M_{11} = \frac{1}{2} \begin{bmatrix} k_x + k_{xD} & -c_1 \\ -c_1 & m \end{bmatrix},$$

$$M_{12} = \frac{1}{2} \begin{bmatrix} k_x + k_{xD} & c_1 \\ c_1 & m \end{bmatrix},$$

and c_1 is a positive constant described in the subsequent analysis. Taking the time derivative of V_1 and substituting the closed-loop dynamics defined in (57) yields

$$\dot{V}_1 = (k_x + k_{xD})e_x \cdot \dot{e}_x + e_v \cdot m \dot{e}_v + c_1 \dot{e}_x \cdot e_v + c_1 e_x \cdot \dot{e}_v$$

Substituting $m \dot{e}_v$ yields

$$\begin{aligned}
\dot{V}_1 = & (k_x + k_{xD})e_x \cdot e_v + e_v \cdot (-(k_x + k_{xD})e_x - (k_v + k_{vD})e_v - X + D_T Re_3) + c_1 \dot{e}_x \cdot e_v \\
& + \frac{c_1 e_x}{m} (-(k_x + k_{xD})e_x - (k_v + k_{vD})e_v - X + D_T Re_3) \\
= & -(k_v - c_1)\|e_v\|^2 - \frac{c_1 k_x}{m}\|e_x\|^2 - \frac{c_1(k_v + k_{vD})}{m}e_x \cdot e_v - X \cdot (\frac{c_1}{m}e_x + e_v) \\
& - k_{xD}\|e_x\|^2 - k_{vD}\|e_v\|^2 + D_T Re_3 \cdot (\frac{c_1}{m}e_x + e_v)
\end{aligned} \tag{82}$$

The upper bound of X can be obtained from the force control input (47), (48), and the desired attitude (52), (49). Rewriting (47) as $f = \vec{f} \cdot Re_3 = (\|\vec{f}\| R_d e_3) \cdot Re_3$ with (52), X becomes upper bounded as follows:

$$\begin{aligned}
X &= \frac{f}{e_3^T R_d^T Re_3} [(e_3^T R_d^T Re_3) Re_3 - R_d e_3] \\
&\leq \frac{\|\vec{f}\| e_3^T R_d^T Re_3}{e_3^T R_d^T Re_3} \|(e_3^T R_d^T Re_3) Re_3 - R_d e_3\|, \\
&\leq \|\vec{f}\| \|(e_3^T R_d^T Re_3) Re_3 - R_d e_3\|
\end{aligned} \tag{83}$$

where the last term $\|(e_3^T R_d^T Re_3) Re_3 - R_d e_3\|$ represents the sine of the angle between Re_3 and $R_d e_3$, and $\|e_R\|$ represents the sine of the eigenaxis rotation angle between R_d and R :

$$\begin{aligned}
\|(e_3^T R_d^T Re_3) Re_3 - R_d e_3\| &\leq \|e_R\| \\
&= \sqrt{\Psi(2 - \Psi)} \\
&\leq \alpha,
\end{aligned} \tag{84}$$

where $\alpha \triangleq \sqrt{\psi_1(2 - \psi_1)} < 1$ based on Proposition 1. Therefore, based on (47) and (84), (83) can be upper bounded by

$$\|X\| \leq ((k_x + k_{xD})\|e_x\| + (k_v + k_{vD})\|e_v\| + B)\|e_R\|. \tag{85}$$

Substituting (85) into (82) yields

$$\begin{aligned}
\dot{V}_1 \leq & - (k_v - c_1) \|e_v\|^2 - \frac{c_1 k_x}{m} \|e_x\|^2 - \frac{c_1 (k_v + k_{vD})}{m} e_x \cdot e_v \\
& + ((k_x + k_{xD}) \|e_x\| + (k_v + k_{vD}) \|e_v\| + B) \|e_R\| (\frac{c_1}{m} \|e_x\| + \|e_v\|) \\
& - k_{xD} \|e_x\|^2 - k_{vD} \|e_v\|^2 + \bar{D}_T \|Re_3\| (\frac{c_1}{m} \|e_x\| + \|e_v\|)
\end{aligned}$$

By the method of completing the square, we know that

$$\begin{aligned}
-k_{xD}(1 - \alpha \frac{c_1}{m}) \|e_x\|^2 + \frac{c_1 \bar{D}_T}{m} \|e_x\| = & -k_{xD}(1 - \alpha \frac{c_1}{m}) (\|e_x\| - \frac{c_1 \bar{D}_T}{2m k_{xD}(1 - \alpha \frac{c_1}{m})})^2 \\
& + \frac{c_1^2 \bar{D}_T^2}{4m^2 k_{xD}(1 - \alpha \frac{c_1}{m})} \\
-k_{vD}(1 - \alpha) \|e_v\|^2 + \bar{D}_T \|e_v\| = & -k_{vD}(1 - \alpha) (\|e_v\| - \frac{\bar{D}_T}{2k_{vD}(1 - \alpha)})^2 \\
& + \frac{\bar{D}_T^2}{4k_{vD}(1 - \alpha)}
\end{aligned}$$

substituting into \dot{V}_1 yields

$$\begin{aligned}
\dot{V}_1 \leq & - (k_v(1 - \alpha) - c_1) \|e_v\|^2 - \frac{c_1 k_x}{m} (1 - \alpha) \|e_x\|^2 \\
& + \frac{c_1 (k_v + k_{vD})}{m} (1 + \alpha) \|e_x\| \|e_v\| + \|e_R\| \left\{ (k_x + k_{xD}) \|e_x\| \|e_v\| + \frac{c_1}{m} B \|e_x\| + B \|e_v\| \right\} \\
& - k_{xD}(1 - \alpha \frac{c_1}{m}) (\|e_x\| - \frac{c_1 \bar{D}_T}{2m k_{xD}(1 - \alpha \frac{c_1}{m})})^2 + \frac{c_1^2 \bar{D}_T^2}{4m^2 k_{xD}(1 - \alpha \frac{c_1}{m})} \\
& - k_{vD}(1 - \alpha) (\|e_v\| - \frac{\bar{D}_T}{2k_{vD}(1 - \alpha)})^2 + \frac{\bar{D}_T^2}{4k_{vD}(1 - \alpha)} \\
\leq & - \begin{bmatrix} \|e_x\| & \|e_v\| \end{bmatrix} \begin{bmatrix} \frac{c_1 k_x}{m} (1 - \alpha) & -\frac{c_1 (k_v + k_{vD})}{2m} (1 + \alpha) \\ -\frac{c_1 (k_v + k_{vD})}{2m} (1 + \alpha) & k_v (1 - \alpha) - c_1 \end{bmatrix} \begin{bmatrix} \|e_x\| \\ \|e_v\| \end{bmatrix} \\
& + \begin{bmatrix} \|e_x\| & \|e_v\| \end{bmatrix} \begin{bmatrix} (k_x + k_{xD}) e_{v_{max}} + \frac{c_1}{m} B & 0 \\ B & 0 \end{bmatrix} \begin{bmatrix} \|e_R\| \\ \|e_\Omega\| \end{bmatrix} \\
& + \frac{c_1^2 \bar{D}_T^2}{4m^2 k_{xD}(1 - \alpha \frac{c_1}{m})} + \frac{\bar{D}_T^2}{4k_{vD}(1 - \alpha)} \\
\leq & -z_1^T W_1 z_1 + z_1^T W_{12} z_2 + \frac{c_1^2 \bar{D}_T^2}{4m^2 k_{xD}(1 - \alpha \frac{c_1}{m})} + \frac{\bar{D}_T^2}{4k_{vD}(1 - \alpha)} \tag{86}
\end{aligned}$$

Proposition 2. *The following inequality is true:*

$$\|e_v(t)\| \leq \max \left\{ \|e_v(0)\|, \frac{B}{k_v(1-\alpha)} \right\} \triangleq e_{v_{\max}}. \quad (87)$$

Proof. Supposing that $c_1 = k_x = k_{xD} = 0$, e_x can drop from (81), and based on it being known that $\|e_R\| \leq 1$, (81) and (86) can be rewritten as

$$V_1 |_{c_1=k_x=k_{xD}=0} = \frac{1}{2}m \|e_v\|^2 \quad (88)$$

$$\begin{aligned} \dot{V}_1 |_{c_1=k_x=k_{xD}=0} &\leq -k_v(1-\alpha) \|e_v\|^2 + B \|e_v\| \\ &\leq -\frac{k_v}{2}(1-\alpha) \|e_v\|^2 \\ &\quad - \frac{k_v}{2}(1-\alpha) \|e_v\|^2 + B \|e_v\| \\ &\leq -\frac{k_v}{2}(1-\alpha) \|e_v\|^2 + \frac{B^2}{2k_v(1-\alpha)}, \end{aligned} \quad (89)$$

where (89) and (88) imply that $\|e_v\|$ is bounded as (87). \square

Based on Proposition 2, \dot{V}_1 can be bounded as

$$\dot{V}_1 \leq -z_1^T W_1 z_1 + z_1^T W_{12} z_2 + \frac{c_1^2 \bar{D}_T^2}{4m^2 k_{xD}(1-\alpha \frac{c_1}{m})} + \frac{\bar{D}_T^2}{4k_{vD}(1-\alpha)}, \quad (90)$$

where W_1, W_{12} are defined as follows:

$$\begin{aligned} W_1 &= \begin{bmatrix} \frac{c_1 k_x}{m} (1-\alpha) & -\frac{c_1 (k_v + k_{vD})}{2m} (1+\alpha) \\ -\frac{c_1 (k_v + k_{vD})}{2m} (1+\alpha) & k_v (1-\alpha) - c_1 \end{bmatrix} \\ W_{12} &= \begin{bmatrix} (k_x + k_{xD}) e_{v_{\max}} + \frac{c_1}{m} B & 0 \\ B & 0 \end{bmatrix}. \end{aligned}$$

To ensure that W_1, M_{11} , and M_{12} are positive definite and $-k_{xD}(1-\alpha \frac{c_1}{m}) < 0$, c_1 is selected to satisfy

$$m < c_1 < \min \left\{ (k_v + k_{vD})(1-\alpha), \frac{4m(k_x + k_{xD})(k_v + k_{vD})(1-\alpha)}{(k_v + k_{vD})^2 (1+\alpha)^2 + 4m(k_x + k_{xD})}, \sqrt{(k_x + k_{xD})m} \right\}, \quad (91)$$

5.3 Stability Analysis of the Overall System

Theorem 2. *The designed controller developed in (47) and (50) ensures that the system defined by (1)–(4) can achieve robust control in the sense of (19) provided that c_1 and c_2 defined in (91) and (65) and the initial condition*

$$\Psi(R(0), R_d(0)) < 1 \quad (92)$$

are satisfied.

Proof. Let $V = V_1 + V_2$ be a Lyapunov function for the system containing rotational and translational dynamics:

$$\begin{aligned} V &= V_1 + V_2 \\ &= \frac{1}{2}(k_x + k_{xD})e_x \cdot e_x + \frac{1}{2}me_v \cdot e_v + c_1 e_x \cdot e_v \\ &\quad + \frac{1}{2}e_\Omega \cdot Je_\Omega + (k_R + k_{RD})\Psi(R, R_d) + c_2 e_R \cdot e_\Omega \end{aligned} \quad (93)$$

It can be shown that (93) is bounded by two positive-definite functions:

$$z_1^T M_{11} z_1 + z_2^T M_{21} z_2 \leq V \leq z_1^T M_{12} z_1 + z_2^T M_{22} z_2$$

Taking the time derivative of (93) and using (75) and (90) yields

$$\begin{aligned} \dot{V} &= \dot{V}_1 + \dot{V}_2 \\ &\leq -z_1^T W_1 z_1 + z_1^T W_{12} z_2 - z_2^T W_2 z_2 \\ &\quad + \frac{c_1^2 \bar{D}_T^2}{4m^2 k_{xD}(1 - \alpha \frac{c_1}{m})} + \frac{\bar{D}_T^2}{4k_{vD}(1 - \alpha)} + \frac{\bar{D}_M^2}{4k_{\Omega D}} + \frac{c_2 \bar{D}_M^2 \lambda_{max}(J)}{4k_{RD} \lambda_{min}^2(J)} \\ &\leq -z_1^T W_1 z_1 + z_1^T W_{12} z_2 - z_2^T W_2 z_2 - z_1^T W_1 z_1 + z_1^T W_{12} z_2 - z_2^T W_2 z_2 \\ &\quad + P_T + P_M \end{aligned}$$

where P_T and P_M are defined as

$$P_T = \frac{c_1^2 \bar{D}_T^2}{4m^2 k_{xD}(1 - \alpha \frac{c_1}{m})} + \frac{\bar{D}_T^2}{4k_{vD}(1 - \alpha)}$$

$$P_M = \frac{\bar{D}_M^2}{4k_{\Omega D}} + \frac{c_2 \bar{D}_M^2 \lambda_{max}(J)}{4k_{RD} \lambda_{min}^2(J)}$$

where W_1, W_{12} are defined in the translational stability analysis and $W_2 \in \mathbb{R}^{2 \times 2}$ is defined in the rotational stability analysis. We expand the \dot{V} as

$$\begin{aligned} \dot{V} &\leq -\lambda_{min}(W_1) \|z_1\|^2 + \|W_{12}\|_2 \|z_1\| \|z_2\| - \lambda_{min}(W_2) \|z_2\|^2 + P_T + P_M \\ &\leq -\frac{1}{2} \lambda_{min}(W_1) \|z_1\|^2 - \frac{1}{2} \lambda_{min}(W_2) \|z_2\|^2 \\ &\quad + \|W_{12}\|_2 \|z_1\|^2 + \|W_{12}\|_2 \|z_2\|^2 - \frac{1}{2} \lambda_{min}(W_1) \|z_1\|^2 - \frac{1}{2} \lambda_{min}(W_2) \|z_2\|^2 \\ &\quad + P_T + P_M. \end{aligned}$$

The following condition must be satisfied to make the terms of \dot{V} except for $(P_T$ and $P_M)$ be negative-definite,

$$\frac{1}{2} \lambda_{min}(W_1) > \|W_{12}\|_2 \tag{94}$$

$$\frac{1}{2} \lambda_{min}(W_2) > \|W_{12}\|_2 \tag{95}$$

and multiplying (94) and (95) yields

$$\lambda_{min}(W_2) > \frac{4 \|W_{12}\|_2^2}{\lambda_{min}(W_1)}$$

As a result, all of the matrices $M_{11}, M_{12}, W_1, M_{21}, M_{22}, W_2$ are positive-definite with appropriate gain selection and the condition $\lambda_{min}(W_2) > \frac{4 \|W_{12}\|_2^2}{\lambda_{min}(W_1)}$ can't guarantee that \dot{V} becomes exponentially stable because the last two terms of \dot{V} (P_T and P_M) are positive terms, but guarantees uniformly ultimately bounded (UUB). Therefore, the whole system is stable, and the error e_x, e_v, e_R, e_Ω are bounded. \square

Chapter 6 Simulations

The simulations were conducted in a professional simulator based on Matlab Simulink[36]. In addition, there is a powerful library in Simulink, which is called Simscape. Simscape enables you to rapidly create models of physical systems within the Simulink environment. Furthermore, a open-source project Quadcopter Drone Model in Simscape has developed by Matlab staff, Steve Miller, was a quadcopter with multibody, electrical and thermal models followed a path to deliver a package. With this well developed project, the present work conducted the motors efficiency estimation. A four-rotor multirotor with an allocation matrix as defined in (24) was used as our model in Simulink with a simulation duration of 50 sec and sampling time 0.01 sec.

6.1 The multirotor

6.1.1 Setup and Ground Truth

The model, motors efficiency, and control gains of the multirotor are presented in Fig. 10, Table 5, and Table 6, respectively. The covariance of process and covariance of measurement are represented in Table 7, and Table 8, respectively. The physical parameters are represented in Table 9. The ground truth of the motors efficiency presented in Table 5 were unknown parameters to be estimated in the simulations, and were used for evaluating the estimate error but not for implementing the simulation.

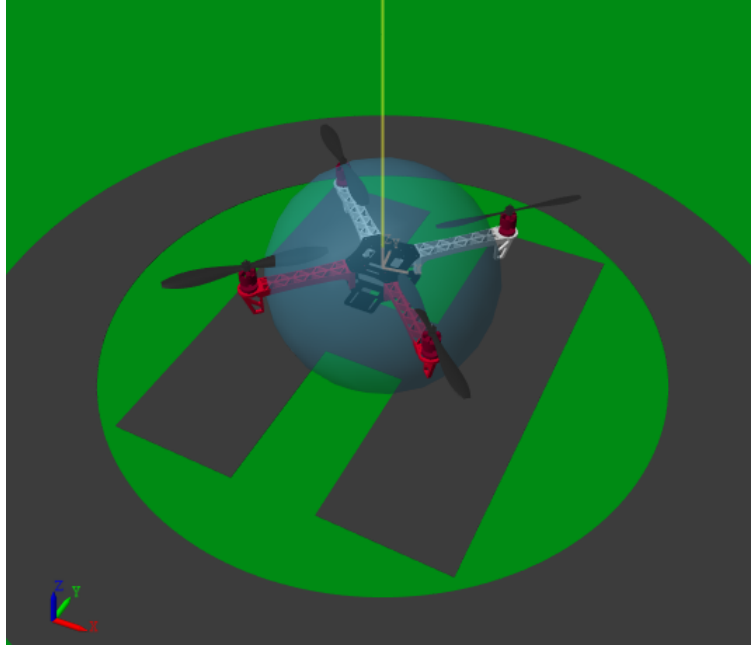


Figure 10: The multirotor model in Simscape. Noted that the yellow line is visualized trajectory and the transparent ball is a visualized waypoint.

Table 5: Ground truth motors efficiency in the Simscape simulations

Parameter	Value
e^1	0.9
e^2	0.7
e^3	0.5
e^4	0.3

The multirotor was initially stationary on the ground and was commanded to track a desired trajectory x_d represented in Fig. 11 and desired yaw direction \vec{X}_{B_d} designed as

$$\vec{X}_{B_d} = \begin{bmatrix} 1 \\ 0 \\ 0 \end{bmatrix},$$

Table 6: Control gains used in the Simscape simulations

Control Gain	Value
$k_x + k_{xD}$	$diag([8, 8, 16])$
$k_v + k_{vD}$	$diag([6, 6, 6])$
$k_R + k_{RD}$	$diag([10, 10, 10])$
$k_\Omega + k_{\Omega D}$	$diag([2.54, 2.54, 2.54])$

Table 7: Covariance of process in the multirotor UKF model in the Simscape simulations

Covariance of process	Value
x_k	10^{-6}
v_k	10^{-6}
a_k	10^{-6}
Ω_k	10^{-6}
α_k	10^{-6}
E_k	10^{-4}

Table 8: Covariance of measurement in the multirotor UKF model in the Simscape simulations

Covariance of measurement	Value
x_k	10^{-6}
Ω_k	10^{-4}

where \vec{X}_{B_d} was chosen to be the unit vector in the direction of the x -axis in the inertial frame.

The initial states and estimates were

$$x(0) = [-2, -2, 0.15],$$

$$v(0) = [0, 0, 0],$$

$$R(0) = \begin{bmatrix} 1 & 0 & 0 \\ 0 & 1 & 0 \\ 0 & 0 & 1 \end{bmatrix},$$

$$\Omega(0) = [0, 0, 0],$$

$$e^1(0) = e^2(0) = e^3(0) = e^4(0) = 1$$

6.1.2 Results

The tracking errors of the position, velocity, attitude, and angular velocity were indeed bounded, as shown in Fig. 12 to Fig. 15. These findings verify that the multirotor with the developed controller and the motors efficiency UKF estimator is able to track a desired trajectory

Table 9: Physical parameters of the multirotor in the Simscape simulations

Parameter	Value	Unit
m	0.952	kg
J	$diag([0.00329, 0.00329, 0.00581])$	$kg \cdot m^2$
l	0.1592	m

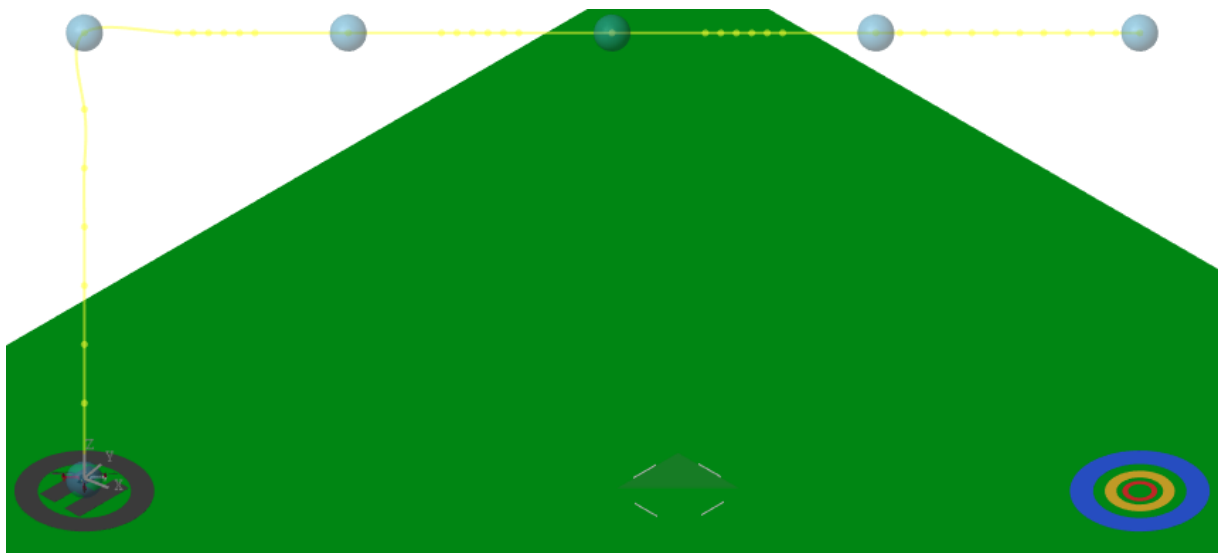


Figure 11: 3D trajectory for the multirotor. Noted that the yellow line is visualized trajectory, the transparent ball is a visualized waypoint, the multirotor is initially stationary on the ground with H, the colorful concentric circles is the end waypoint projection on the ground.

without knowledge of the motors efficiency. The $(\cdot)_1$, $(\cdot)_2$, and $(\cdot)_3$ notations in the following figures represent the first, second, and third elements of the corresponding vector, respectively.

Position Errors

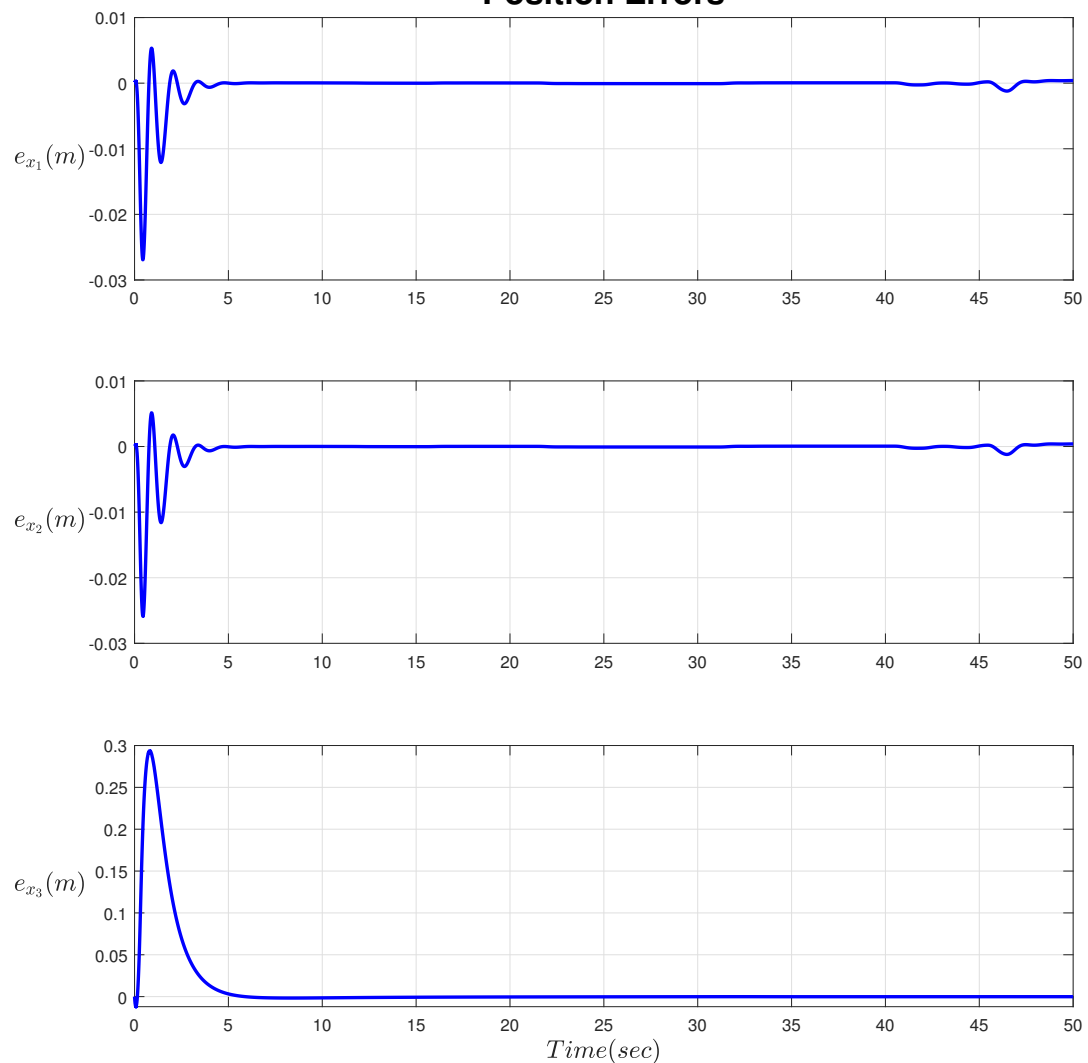


Figure 12: Position error

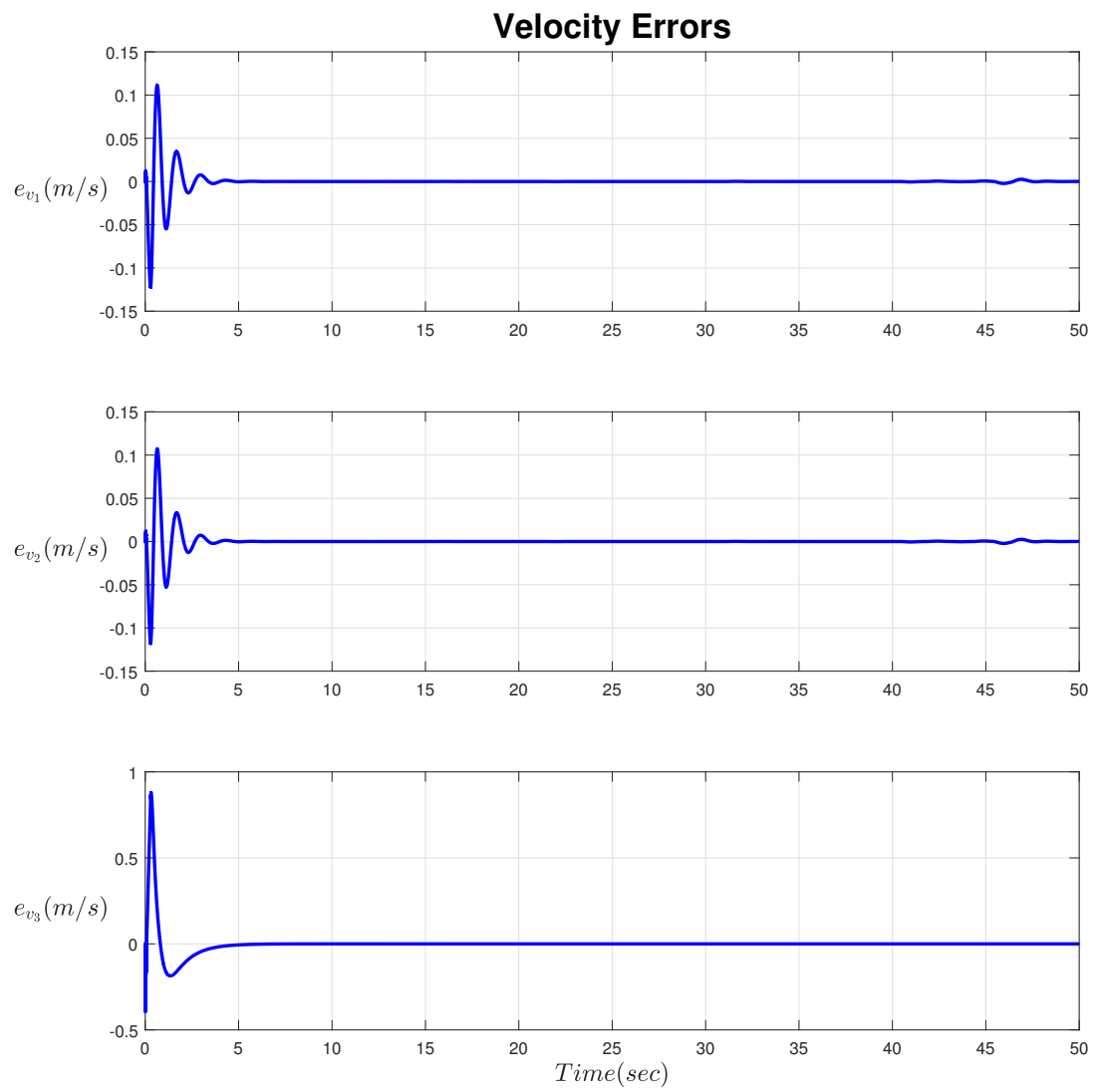


Figure 13: Velocity error

The attitude error and the angular velocity error defined in (17) and (18) are shown in Fig. 14 and Fig. 15, respectively.

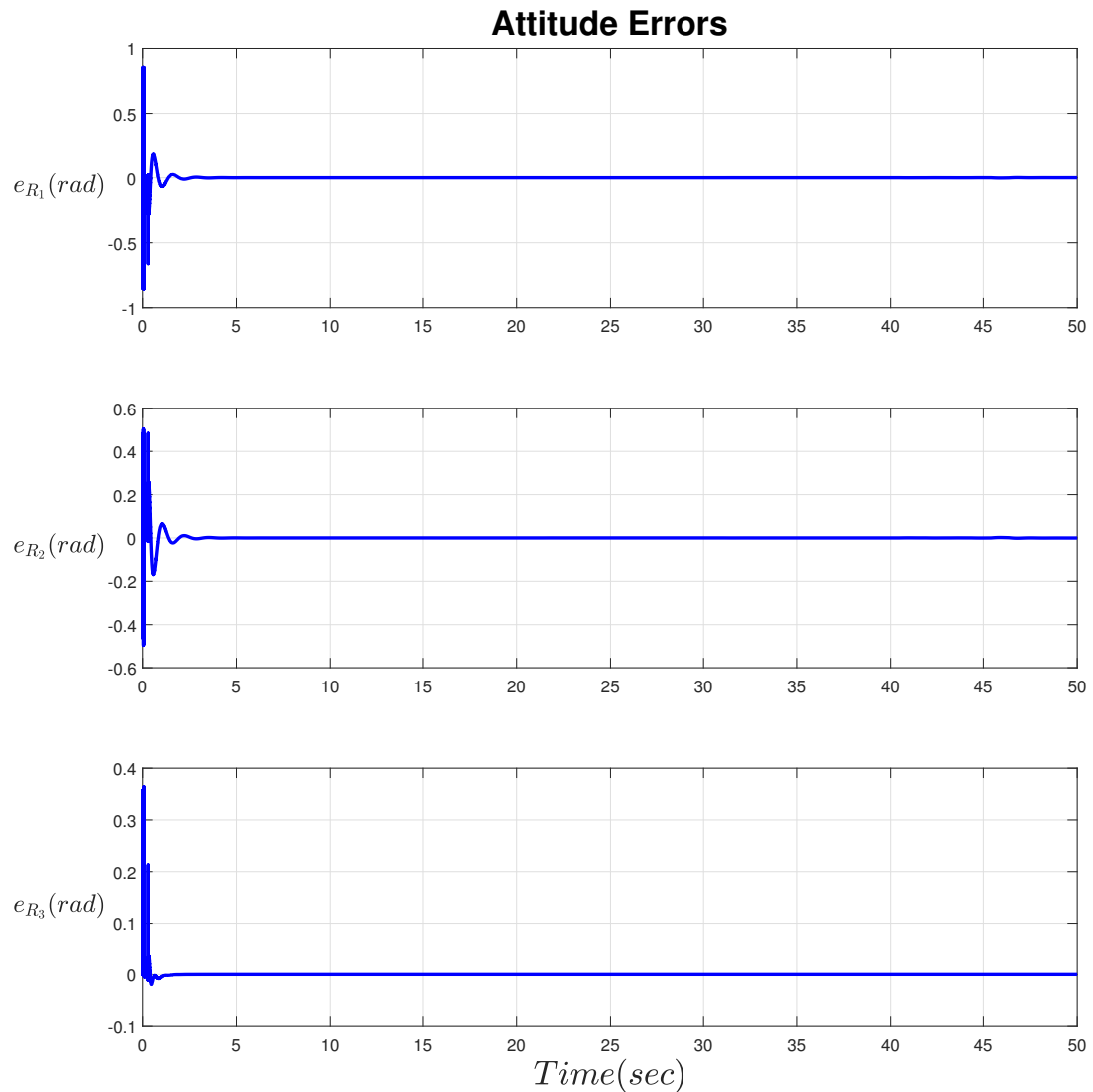


Figure 14: Attitude error

Angular Velocity Errors

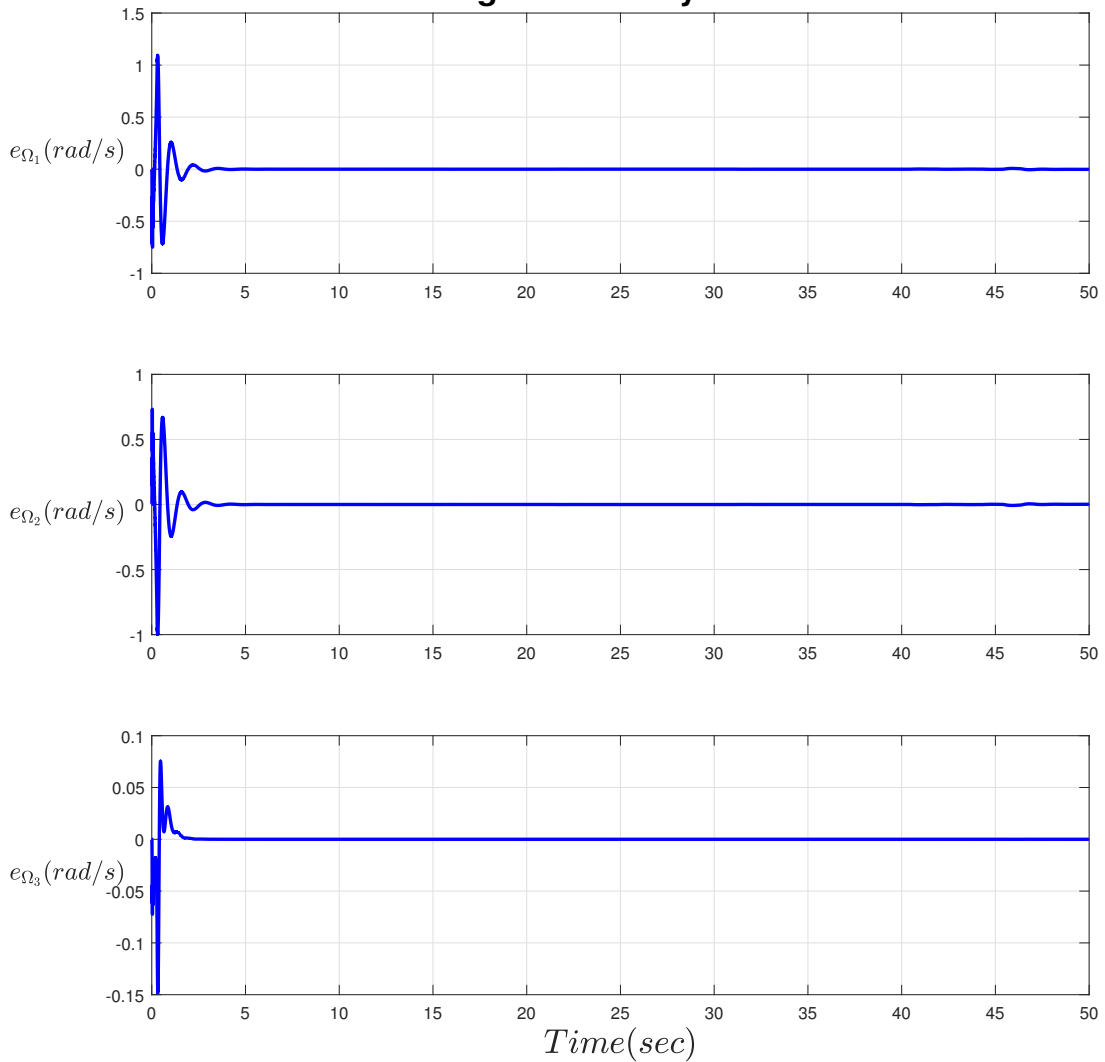


Figure 15: Angular velocity

Fig. 16 shows the estimates of the motors efficiency during flight. The estimated values of the motors efficiency are 0.9, 0.7, 0.5, 0.3 after about 3 sec, which are very close to the ground truth listed in Table 5.

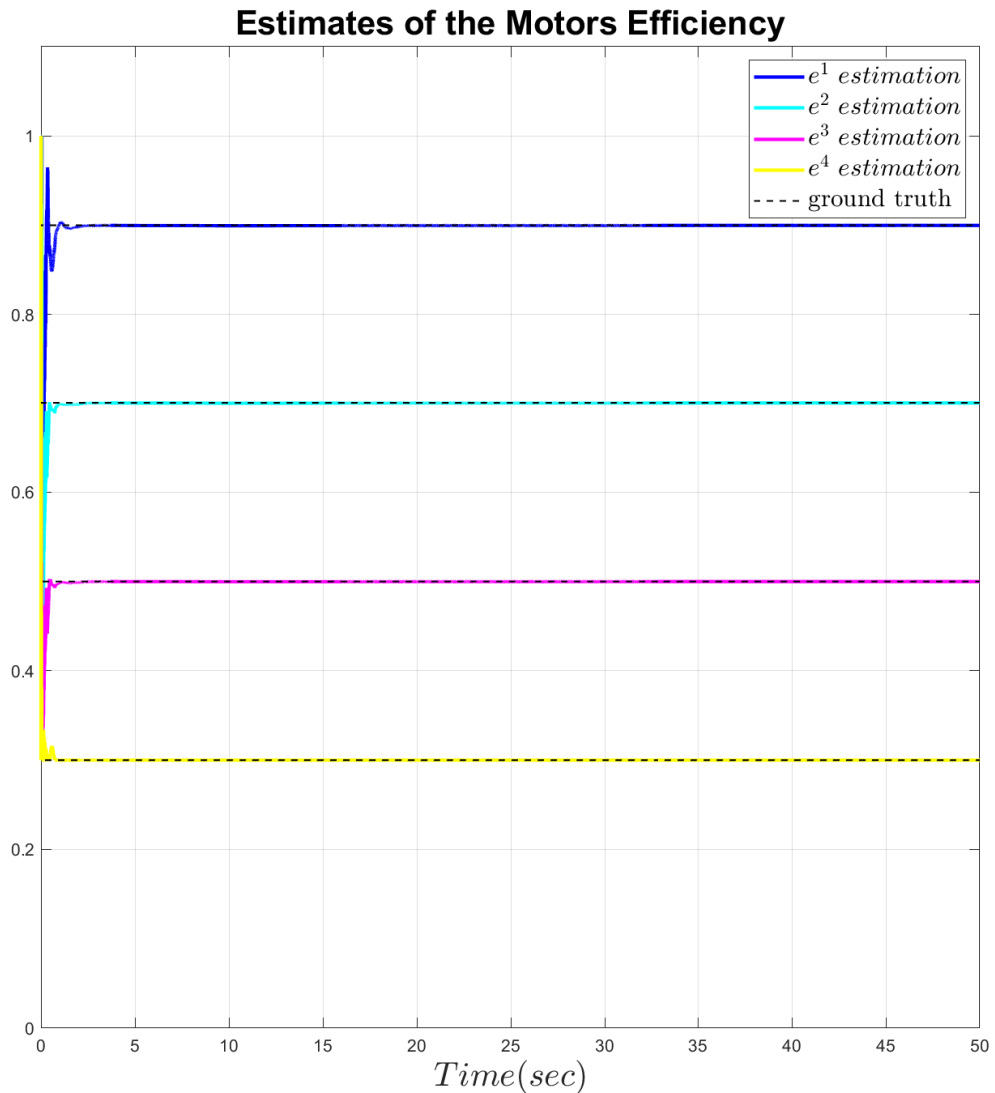


Figure 16: Estimates of the motors efficiency.

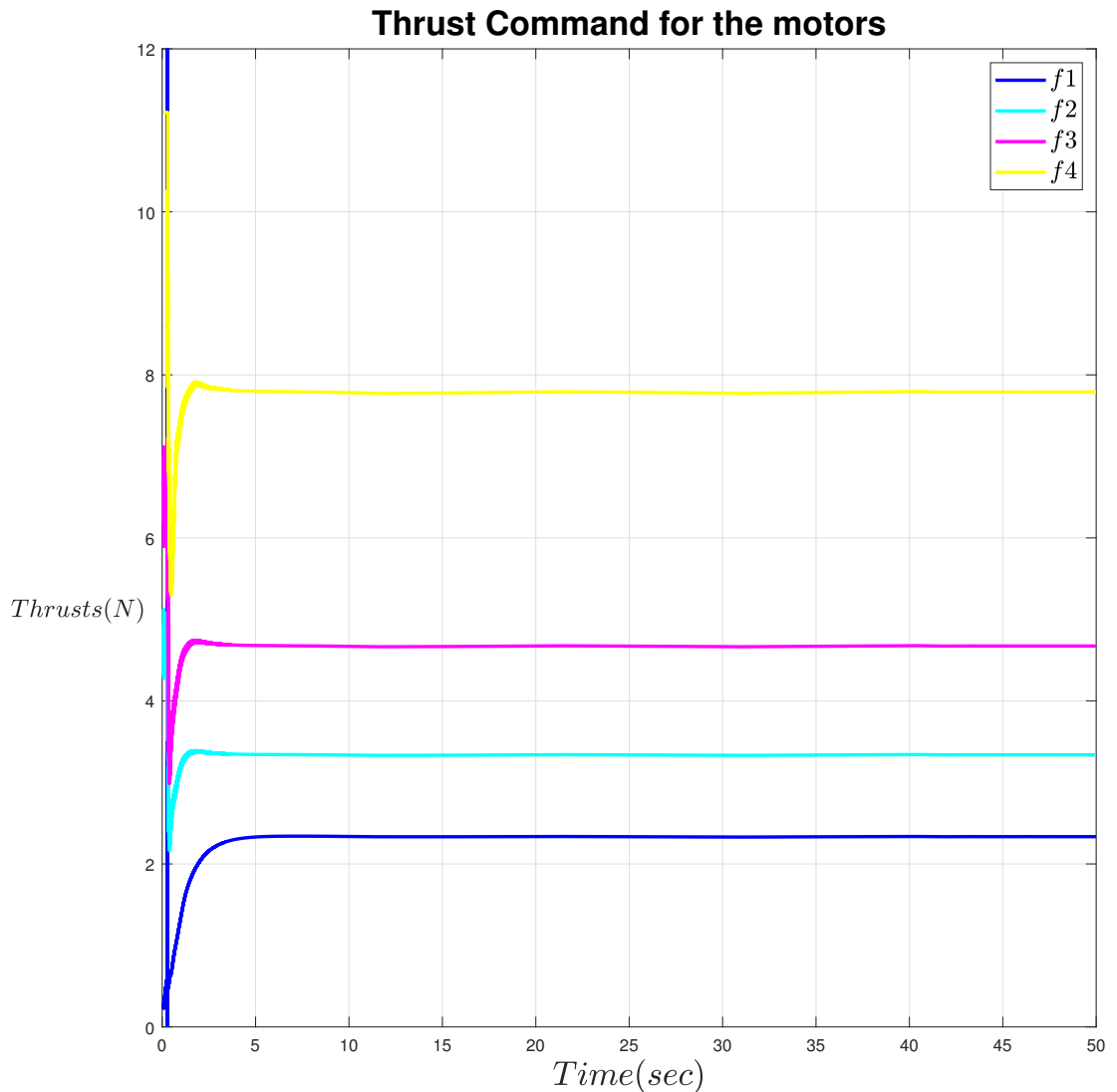


Figure 17: Thrust command for the motors

Fig. 17 shows that the system of developed control and motors efficiency UKF estimator truly generates the bigger thrust command to compensate the defective motors. The ratios between the normal thrust command ($2.33N$) and the thrust command for defective motors are the reciprocal of the estimated motors efficiency, that is $\frac{1}{0.9}, \frac{1}{0.7}, \frac{1}{0.5}, \frac{1}{0.3}$.

Fig. 18 compares the position with and without the motors efficiency feedback. The position with the motors efficiency feedback almost overlaps with the trajectory, whereas the position without the motors efficiency feedback has an obvious error.

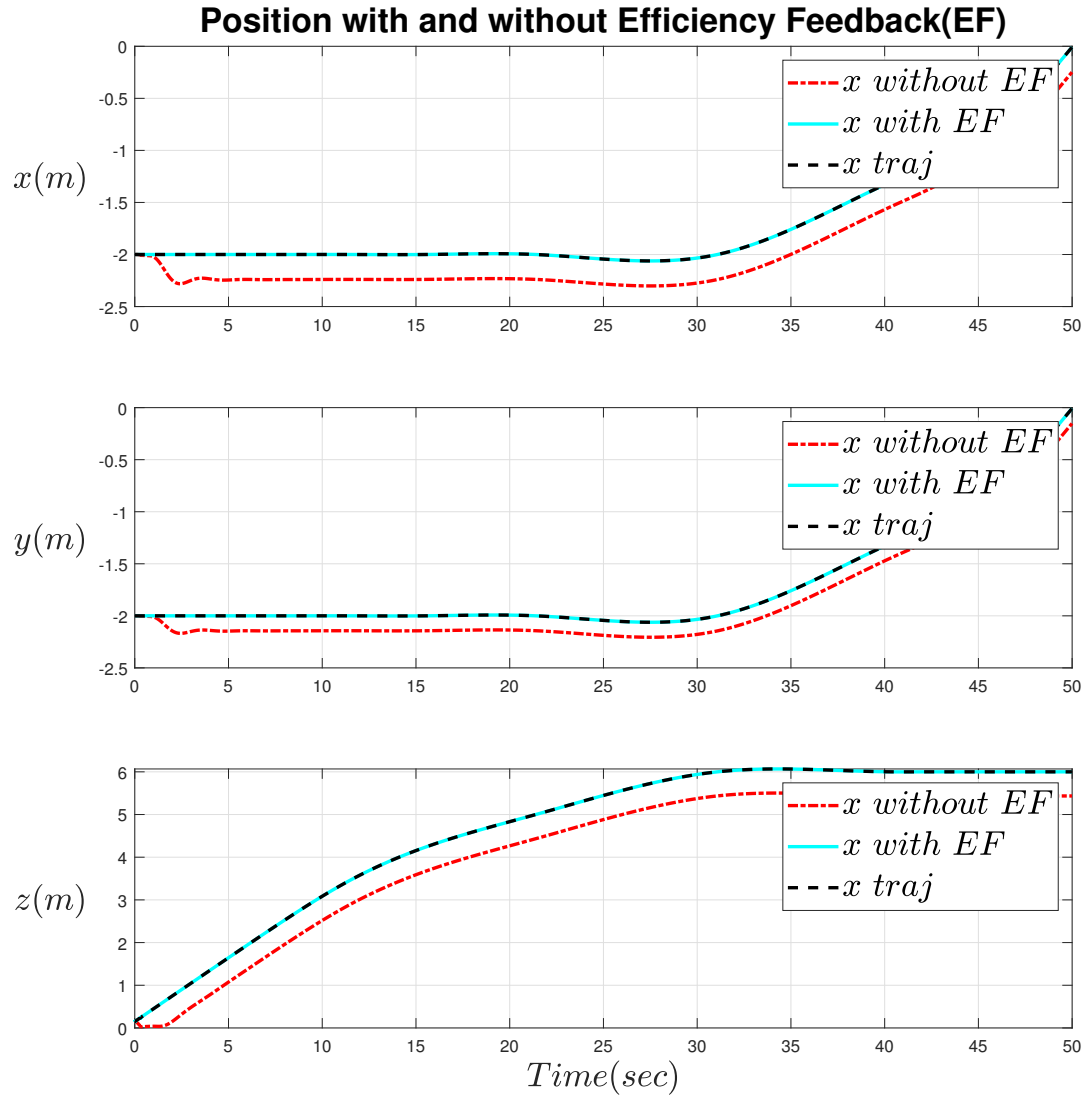


Figure 18: Comparison of the position with and without the Motors Efficiency Feedback.

6.2 The Cooperative Transportation System

6.2.1 Setup and Ground Truth

The model, motors efficiency, and control gains of the CTS are presented in Fig. 19, Table 10, and Table 11, respectively. The covariance of process and covariance of measurement are represented in Table 12, and Table 13, respectively. The physical parameters are represented in Table 14. The ground truth of the motors efficiency presented in Table 10 were unknown parameters to be estimated in the simulations, and were used for evaluating the estimate error but not for implementing the simulation. Notice that the motors efficiency estimation was not conducted in realtime, because the error of the feedback motors estimation caused the CTS had a severe dynamics. A severe dynamics in Simscape leads to a very long time calculation, which significantly influences the simulations. Therefore, the estimation of motors efficiency was conducted offline. Although the simulations failed in the realtime feedback step, the control and offline estimation performance were still presented below.

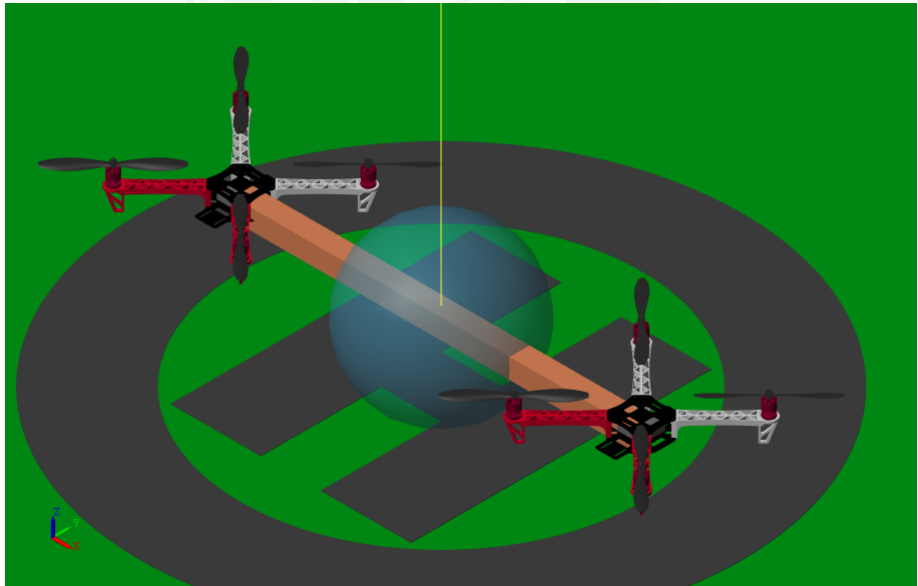


Figure 19: The multirotor model in Simscape. Noted that the yellow line is visualized trajectory and the transparent ball is a visualized waypoint.

Table 10: The CTS Ground truth motors efficiency in the Simscape simulations

Parameter	Value
e_1^1	0.75
e_1^2	0.55
e_1^3	0.45
e_1^4	0.65
e_2^1	0.5
e_2^2	0.6
e_2^3	0.8
e_2^4	0.7

Table 11: Control gains used in the Simscape simulations

Control Gain	Value
$k_x + k_{xD}$	$diag([4, 4, 15])$
$k_v + k_{vD}$	$diag([4, 4, 10])$
$k_R + k_{RD}$	$diag([16, 40, 8])$
$k_\Omega + k_{\Omega D}$	$diag([2.54, 2.54, 2.54])$

The CTS was initially stationary on the ground and commanded to track a desired trajectory x_d represented in Fig. 20 and desired yaw direction \vec{X}_{B_d} designed as

$$\vec{X}_{B_d} = \begin{bmatrix} 1 \\ 0 \\ 0 \end{bmatrix},$$

where \vec{X}_{B_d} is chosen to be the unit vector in the direction of the x -axis in the inertial frame.

Table 12: Covariance of process in the CTS UKF model in the Simscape simulations

Covariance of process	Value
$x_{1,k}$	10^{-6}
$v_{1,k}$	10^{-4}
$a_{1,k}$	10^{-2}
$\Omega_{1,k}$	10^{-6}
$\alpha_{1,k}$	10^{-2}
$E_{1,k}$	10^{-6}
$x_{2,k}$	10^{-6}
$v_{2,k}$	10^{-4}
$a_{2,k}$	10^{-2}
$\Omega_{2,k}$	10^{-6}
$\alpha_{2,k}$	10^{-2}
$E_{2,k}$	10^{-6}
$F_{1,k}$	25
$F_{2,k}$	25

Table 13: Covariance of measurement in the CTS UKF model in the Simscape simulations

Covariance of measurement	Value
$x_{1,k}$	10^{-6}
$\Omega_{1,k}$	10^{-6}
$\tau_{1,k}$	10^{-6}
$x_{2,k}$	10^{-6}
$\Omega_{2,k}$	10^{-6}
$\tau_{2,k}$	10^{-6}

Table 14: Physical parameters of the CTS in the Simscape simulations

Parameter	Value	Unit
m_1, m_2	0.952	kg
m_p	0.5	kg
m_s	2.404	kg
J_1, J_2	$diag([0.00329, 0.00329, 0.00581])$	$kg \cdot m^2$
J_p	$diag[0.0002, 0.042, 0.042])$	$kg \cdot m^2$
J_s	$diag([0.068, 0.5244, 0.5294])$	$kg \cdot m^2$
l	0.1592	m
r	0.5	m

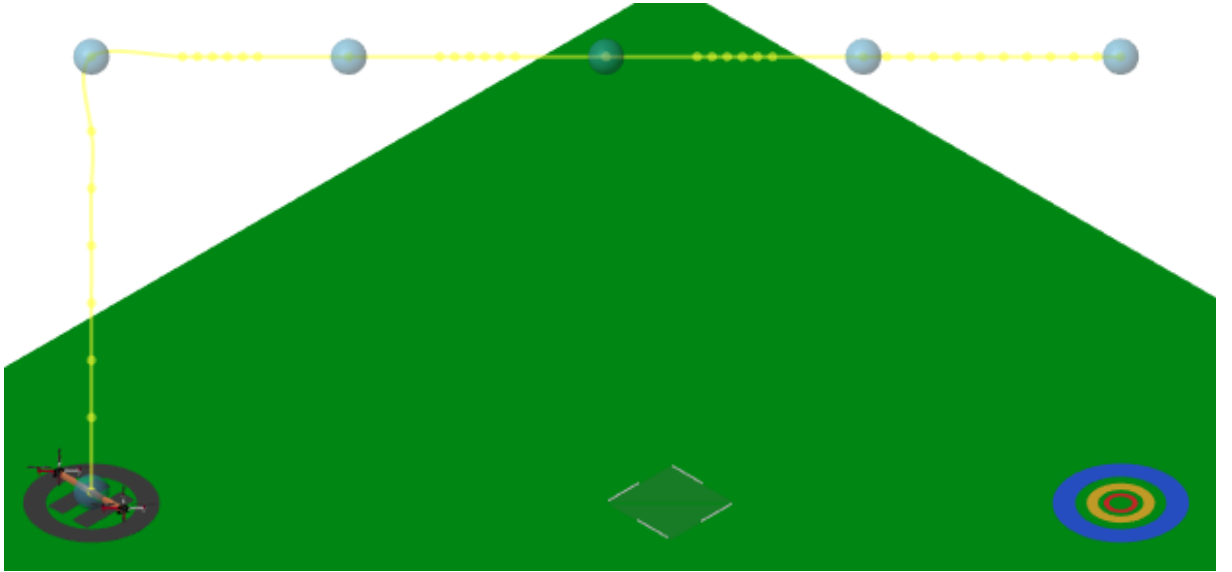


Figure 20: 3D trajectory for the CTS. Noted that the yellow line is visualized trajectory, the transparent ball is a visualized waypoint, the CTS is initially stationary on the ground with H, the colorful concentric circles is the end waypoint projection on the ground.

The initial states and estimates were

$$x_1(0) = [-2.5, -2, 0.15],$$

$$v_1(0) = [0, 0, 0],$$

$$R(0) = \begin{bmatrix} 1 & 0 & 0 \\ 0 & 1 & 0 \\ 0 & 0 & 1 \end{bmatrix},$$

$$\Omega(0) = [0, 0, 0],$$

$$e_1^1(0) = e_1^2(0) = e_1^3(0) = e_1^4(0) = 1$$

$$x_2(0) = [-1.5, -2, 0.15],$$

$$v_2(0) = [0, 0, 0],$$

$$e_2^1(0) = e_2^2(0) = e_2^3(0) = e_2^4(0) = 1$$

$$x_p(0) = [-2, -2, 0.15],$$

$$v_p(0) = [0, 0, 0]$$

6.2.2 Result

The tracking errors of the position, velocity, attitude, and angular velocity were indeed bounded, as shown in Fig. 21 to Fig. 24. These findings verify that the CTS with the developed

controller is able to track a desired trajectory with normal motors, and the UKF estimator is able to estimate the motors efficiency. The $(\cdot)_1$, $(\cdot)_2$, and $(\cdot)_3$ notations in the following figures represent the first, second, and third elements of the corresponding vector, respectively.

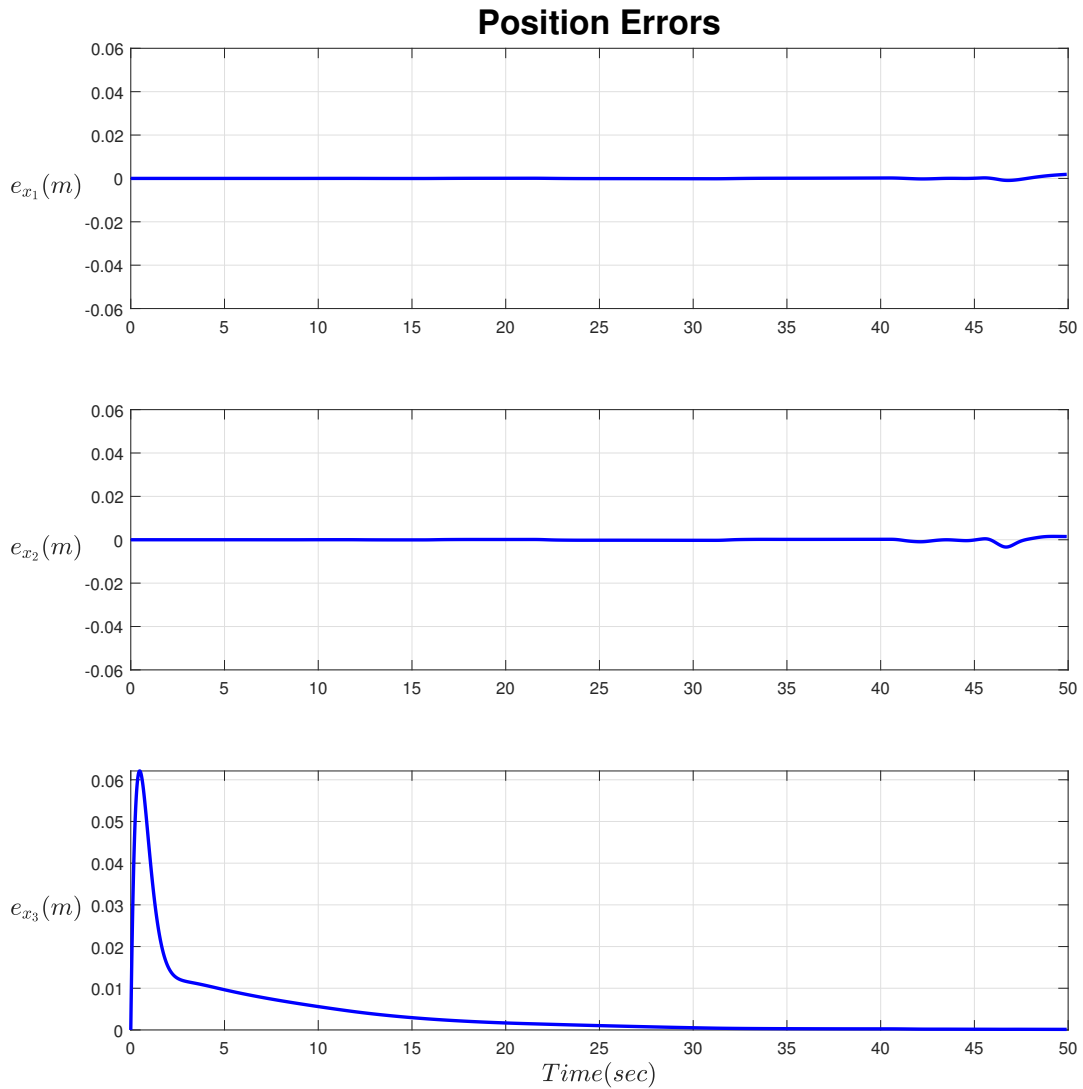


Figure 21: The CTS position error

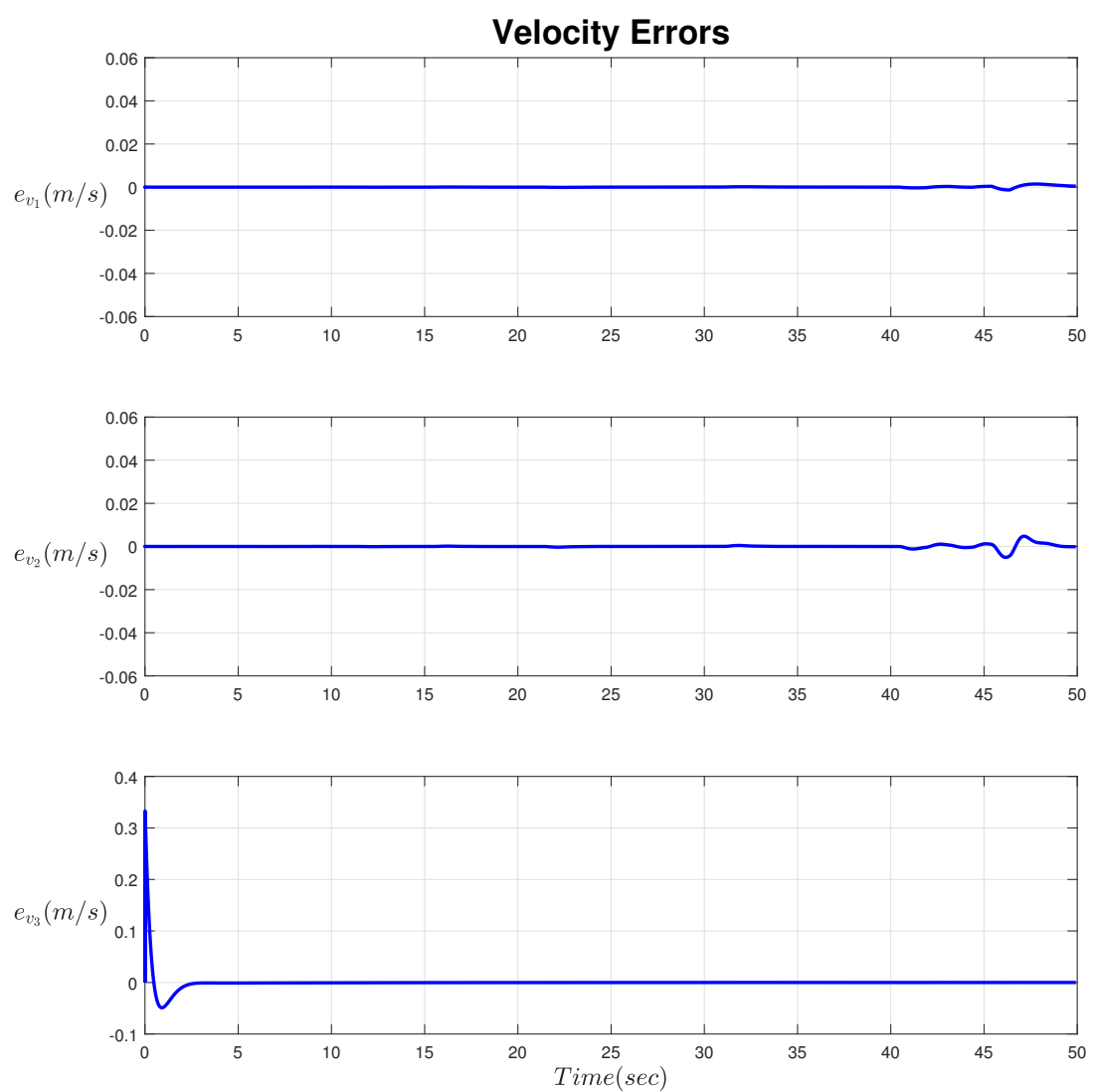


Figure 22: Velocity error

The attitude error and the angular velocity error defined in (17) and (18) are shown in Fig. 23 and Fig. 24, respectively.

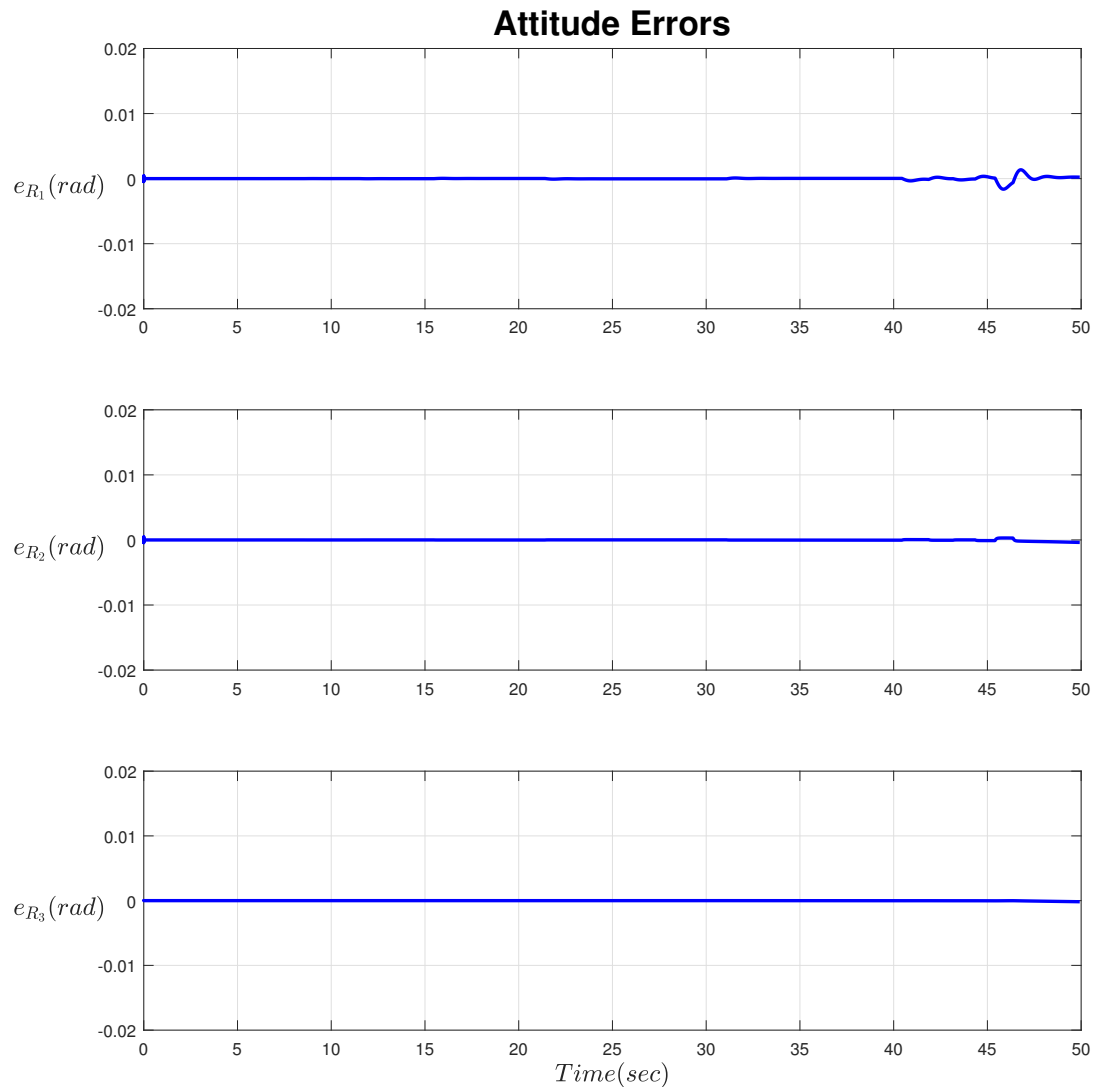


Figure 23: Attitude error

Angular Velocity Errors

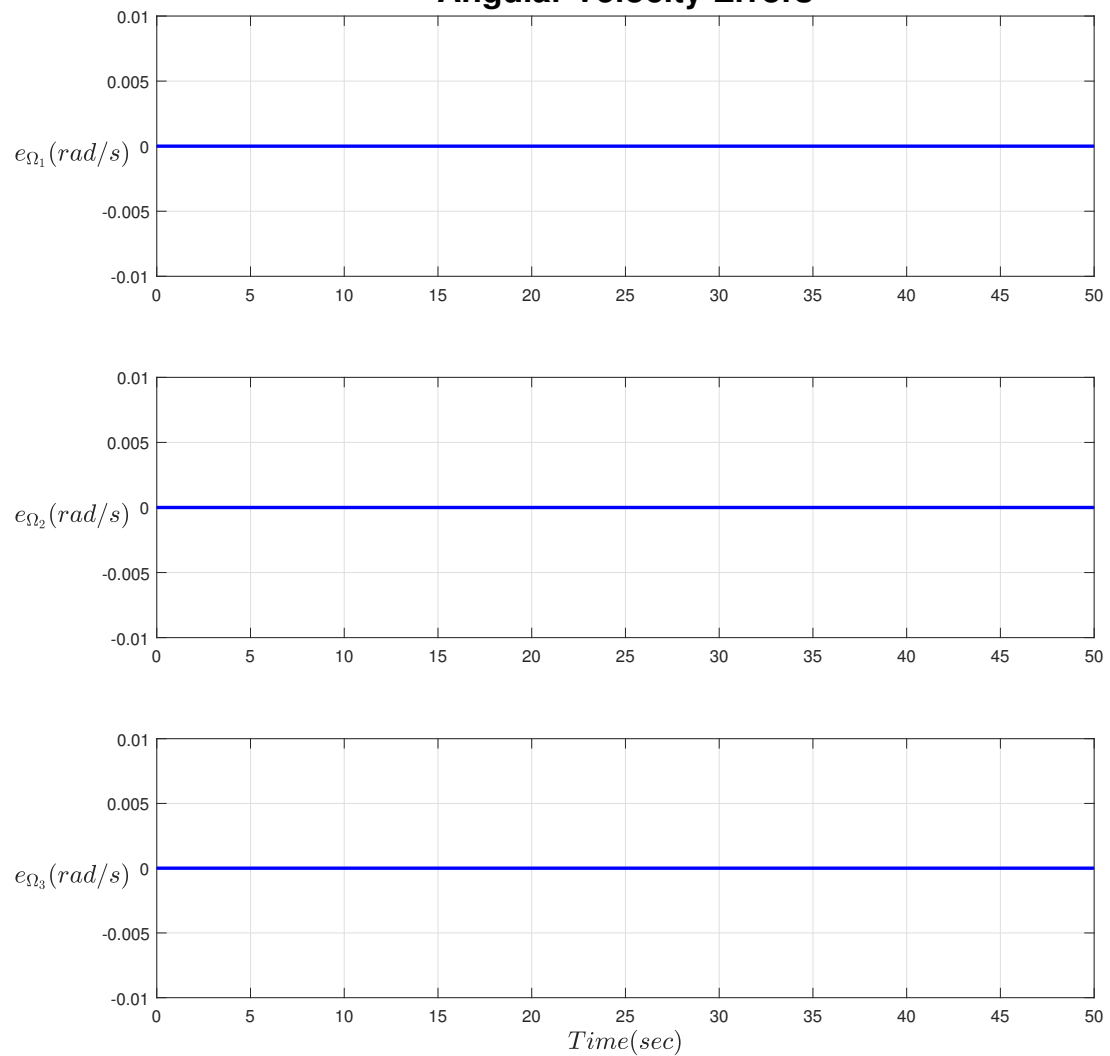


Figure 24: Angular velocity

Fig. 25 and Fig. 26 show the offline estimates of the motors efficiency. The estimated values of the q_1, q_2 motors efficiency are very close to the ground truth motors efficiency listed in Table 10 after about 10 sec.

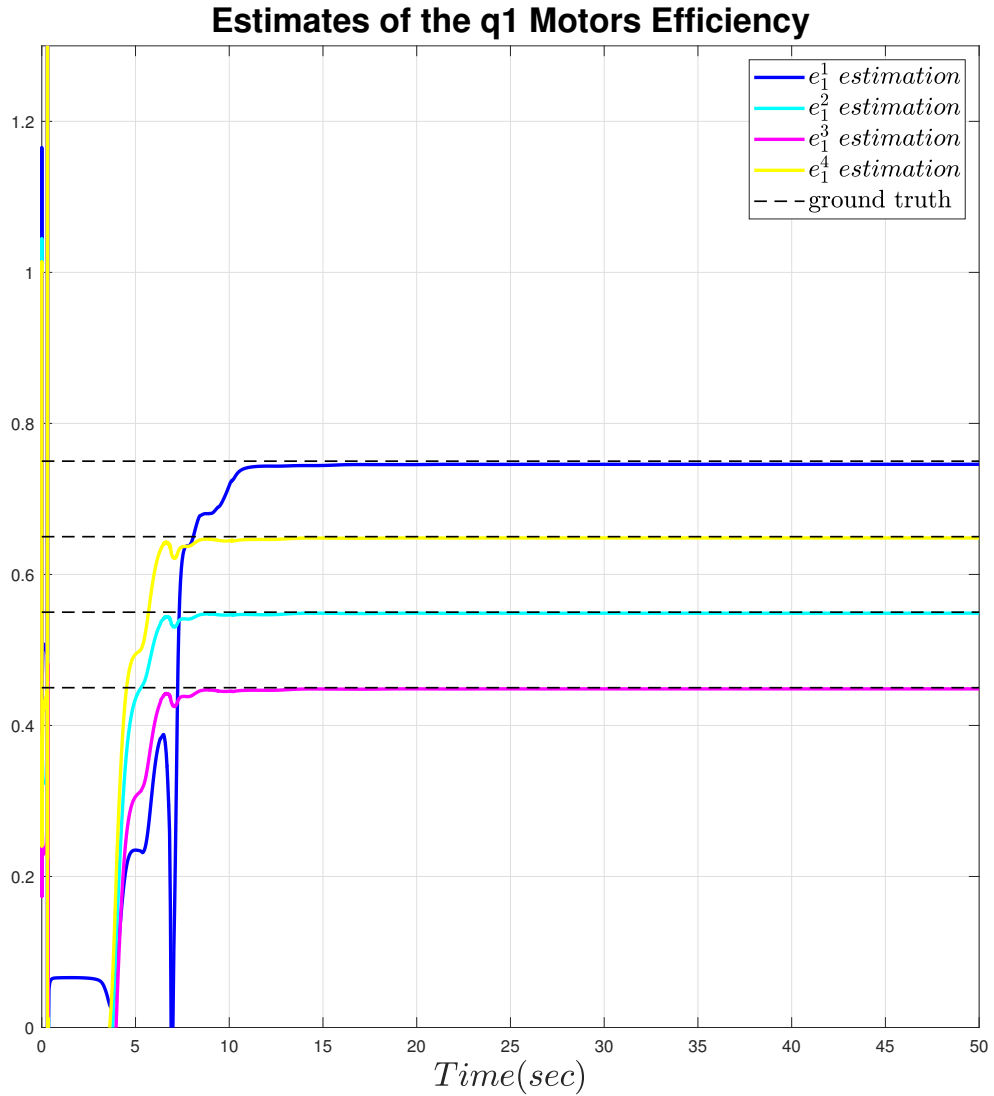


Figure 25: Estimates of the q_1 motors efficiency

Estimates of the q2 Motors Efficiency

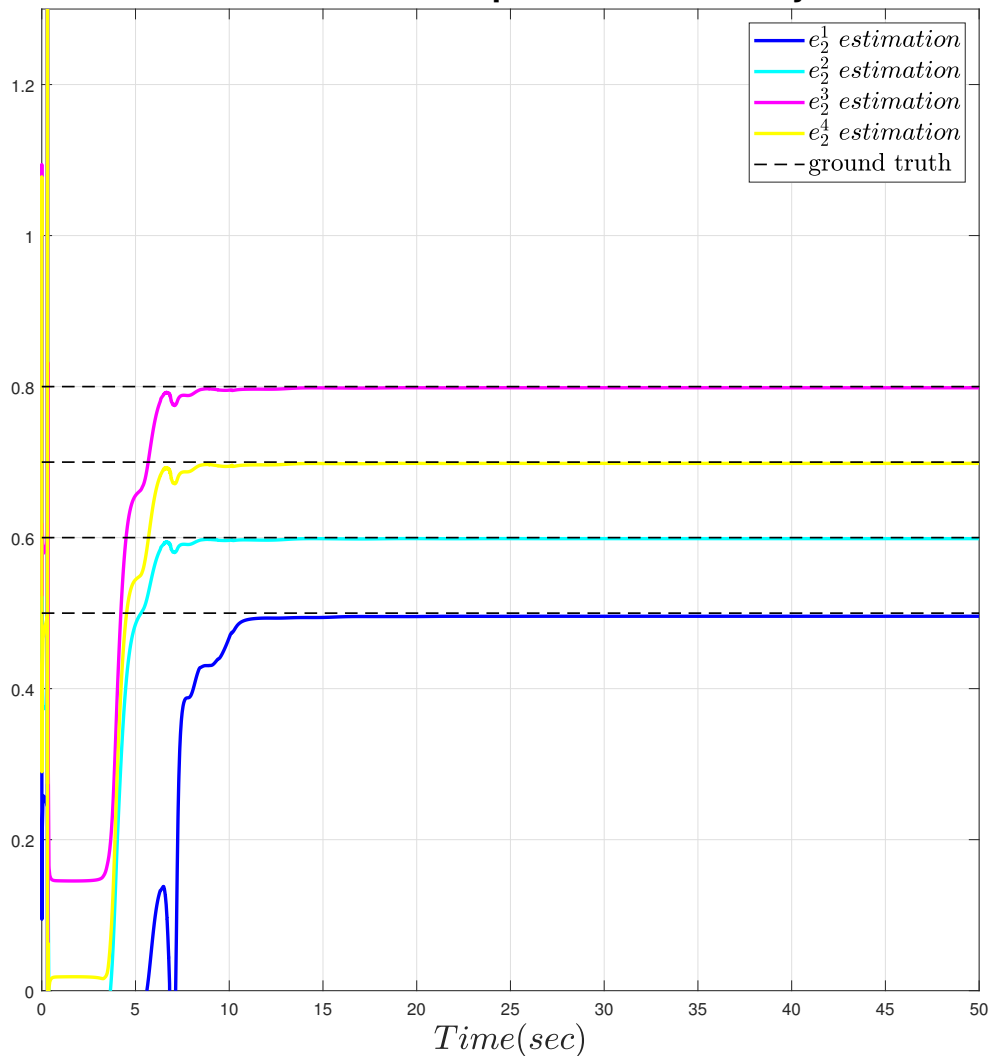


Figure 26: Estimates of the q2 motors efficiency

Fig. 27 compares the position with normal motors or defective motors. The position with the normal motors almost overlaps with the trajectory, whereas the position with the defective motors has obvious error.

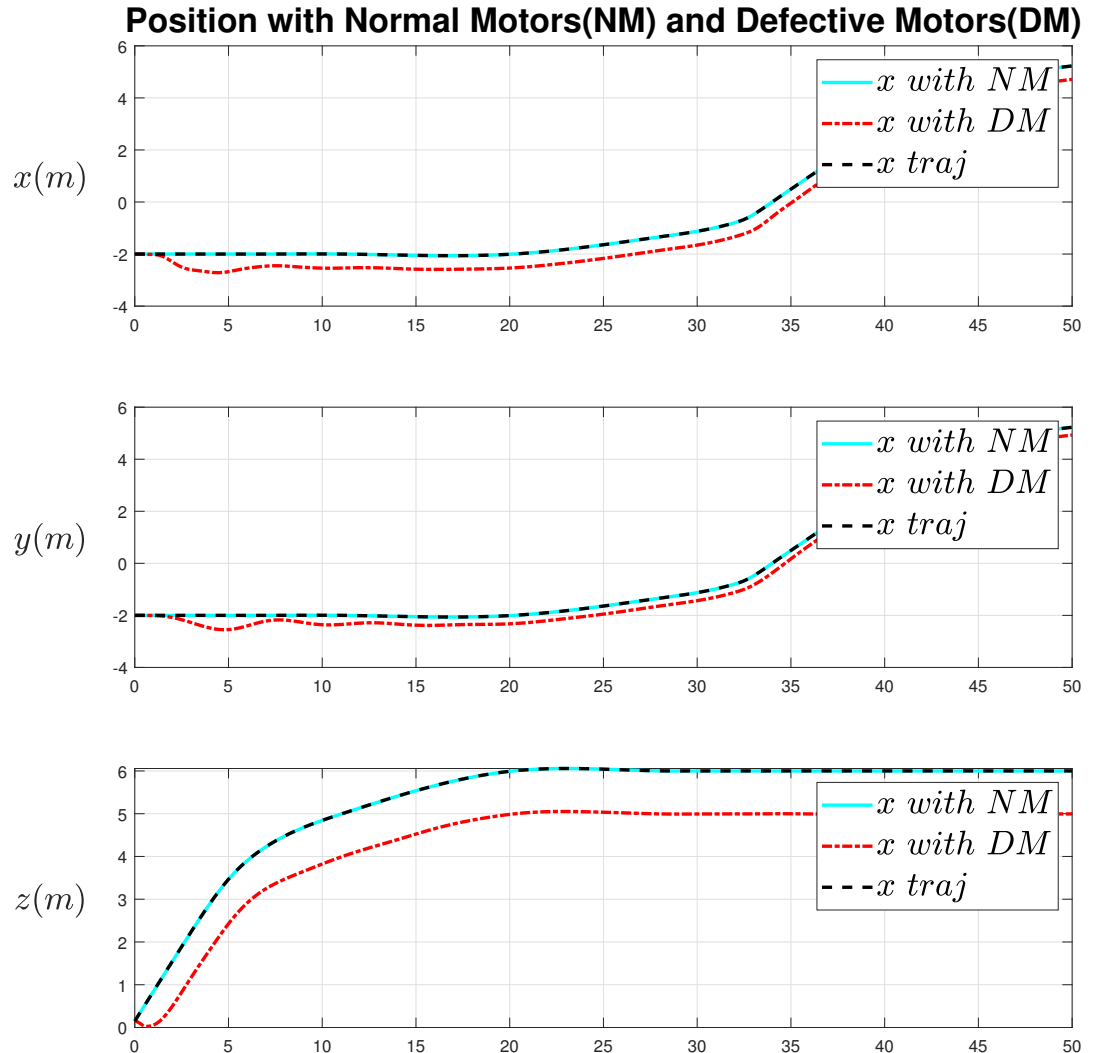


Figure 27: Comparison of the position with and without the Motors Efficiency Feedback.

Chapter 7 Experiments

7.1 The Multirotor

In this section, the experimental results using developed controller are presented. We used a four-rotor multirotor with an allocation matrix defined as

$$\begin{bmatrix} f \\ M_x \\ M_y \\ M_z \end{bmatrix} = \begin{bmatrix} 1 & 1 & 1 & 1 \\ -l & l & l & -l \\ l & l & -l & -l \\ -c_{\tau f} & c_{\tau f} & -c_{\tau f} & c_{\tau f} \end{bmatrix} \begin{bmatrix} f_1 \\ f_2 \\ f_3 \\ f_4 \end{bmatrix}$$

in the flight experiments. We show the accuracy of the UKF estimator and demonstrate the ability of the developed controller with the feedback of the motors efficiency to track a desired trajectory. Moreover, the comparison between geometric tracking controller with and without the motors efficiency feedback is presented.

7.1.1 Hardware Architecture

A DJI F450 frame of multirotor is deployed as the hardware architecture to implement the developed controller and the UKF estimator system in the experiments. XBee modules are equipped to the multirotor to communicate between the multirotor and the ground station. Angular velocity and acceleration for obtaining the attitude of the multirotor are measured from inertial measurement unit (IMU), and the position of the multirotor is measured from motion capture system (Optitrack) with 12 cameras. The configuration of the multirotor is shown in Fig. 28.



Figure 28: The Multirotor Hardware architecture.

The ground truth parameters, control gains, and parameters used in the developed controller are listed in Table 15, Table 16, respectively. The ground truth of moment of inertia was obtained by establishing the physical model of the multirotor in the Simscape environment and the ground truth of mass was measured on the scales. The value of moment of inertia J and mass m are represented in Table 15.

Table 15: Parameters used in the experiments

Parameter	Value	Unit
m	1.42	kg
J	$\text{diag}([0.012, 0.012, 0.022])$	$\text{kg} \cdot \text{m}^2$
l	0.1625	m

Table 16: Control gains used in the experiments

Parameter	Value
$k_x + k_{xD}$	$\text{diag}([8.8, 8.8, 15])$
$k_v + k_{vD}$	$\text{diag}([4, 4.4, 10])$
$k_R + k_{RD}$	$\text{diag}([2.95, 2.95, 28.4])$
$k_\Omega + k_{\Omega D}$	$\text{diag}([0.36, 0.36, 1.15])$

7.1.2 Trajectory Generation

To generate a smooth desired trajectory for the multirotor, [37] formulated the trajectory generation problem as a quadratic programming (QP) problem. We write the trajectory passing

through given waypoints as piecewise polynomial function of order n as

$$s_i(t) = \sum_{j=0}^n \sigma_{ij} t^j, t_{i-1} \leq t < t_i, i \in \{1, 2, \dots, m\},$$

where $n = 7$ is selected to obtain the minimum-snap trajectory, $m \in \mathbb{N}$ is the total numbers of segments of the trajectory, $\sigma_{ij} \in \mathbb{R}$ is the coefficient of j^{th} order of the polynomial. The quadratic problem for the minimum-snap trajectory is written with the cost function and the constraints involving initial condition, final condition, and the intermediate condition as

$$\begin{aligned} \min \int_{t_0}^{t_m} \left\| \frac{d^4 s_i}{dt^4} \right\|^2 dt, \\ \text{s.t. } A\sigma = b. \end{aligned}$$

7.1.3 Estimate of the Motors Efficiency

In order to mimic the fault condition, the motors efficiency were set as 1, 0.7, 0.7, 1 respectively, which was shown in Fig. 29.

The estimate of the motors efficiency of the multirotor was estimated as and shown in Fig. 30 which had $\pm 10\%$ error. The result in Fig. 30 shows that the multirotor with the developed UKF estimator is able to estimate the motors efficiency during the flight.

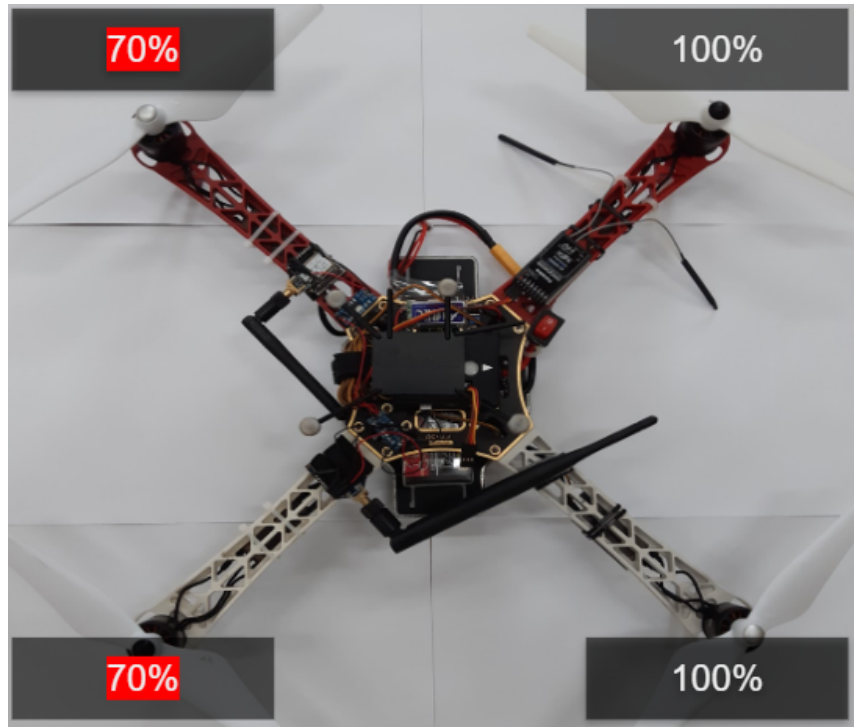


Figure 29: The fault condition of the motors efficiency

陽明交大
NYCU

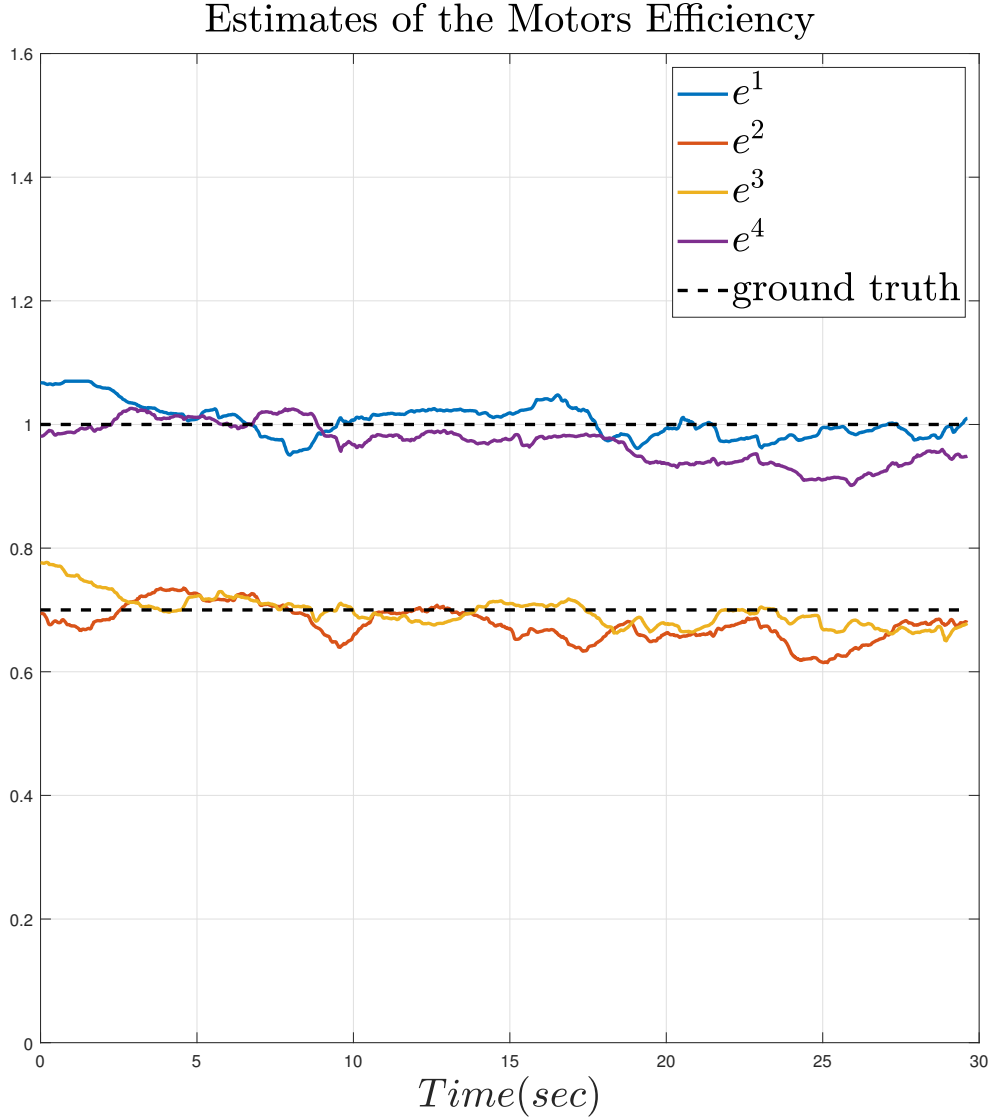


Figure 30: Estimates of the motors efficiency of the multirotor in the experiments. The dotted line represents the ground truth.

7.1.4 Tracking Performance

After a minimum-snap trajectory being generated in Section. 7.1.2, we test our developed controller, UKF estimator and the motors efficiency feedback two runs of the trajectory. The two dimensions heart trajectory tracking performance are presented in Fig. 31. In Fig. 31, the Reference line represents the position trajectory that the multirotor with normal motors tracks the planned trajectory, the Defective Motors line represents the position trajectory that the multirotor with defective motors shown in Fig. 29 tracks the planned trajectory, the Defective Motors with Feedback line represents the position trajectory that the multirotor with defective motors shown

in Fig. 29 tracks the planned trajectory with the feedback estimated motors efficiency. According to the fault condition in Fig. 29, it's obvious that the left side motors have the less thrust, and that's why the position trajectory that the multirotor with defective motors skewes to the left.

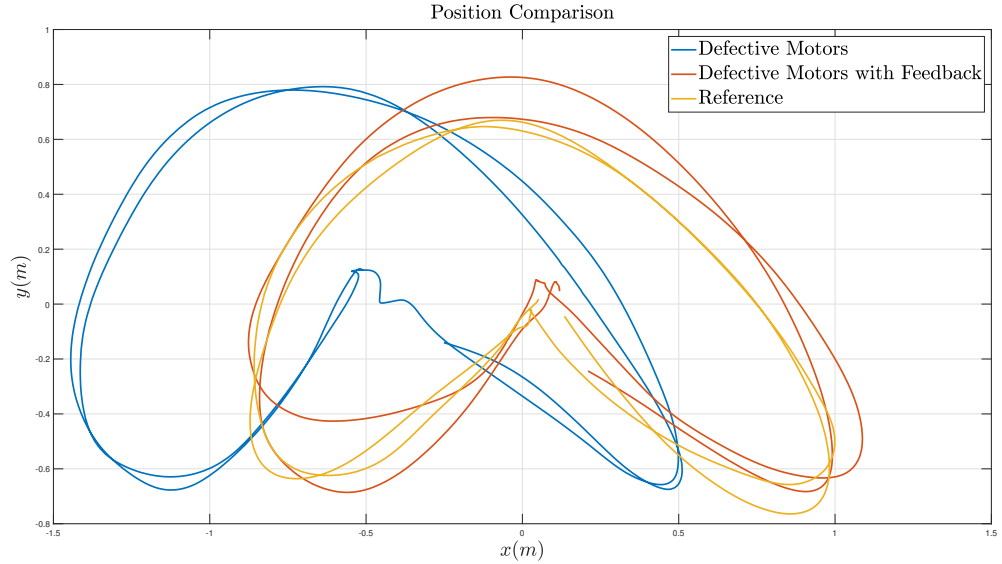


Figure 31: Tracking performance of the 2D position

Fig. 32 and 33 shows the details of the tracking performance of the position X direction and position Z direction. These findings verify that the multirotor with the developed controller and estimator is able to track a desired trajectory without knowledge of the motors efficiency.

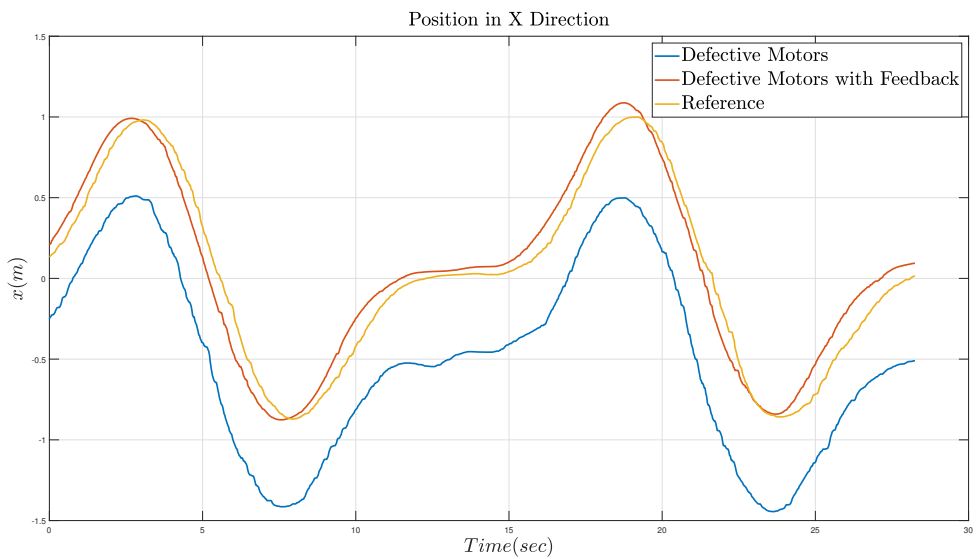


Figure 32: Tracking performance of the position X direction.

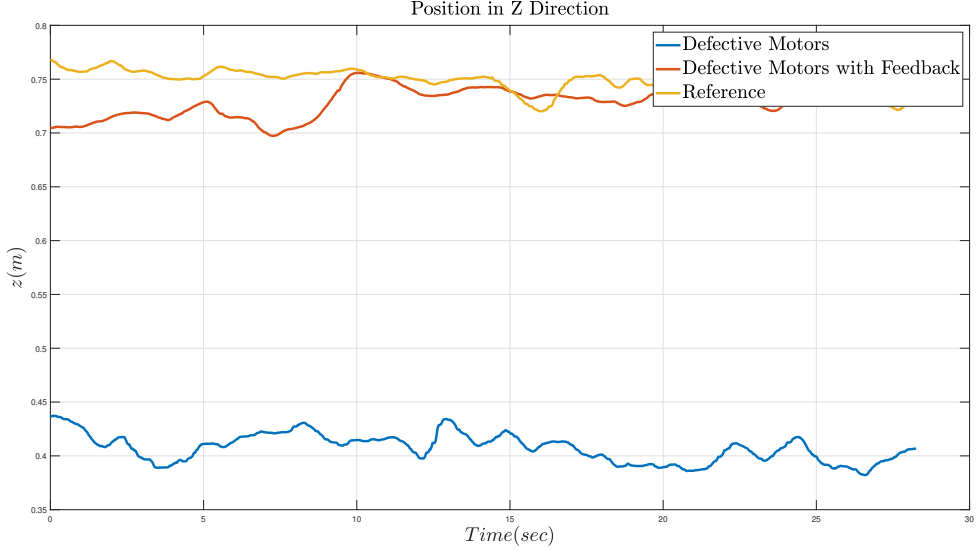


Figure 33: Tracking performance of the position in Z direction.

In Fig. 34, we can see the thrust commands for Motor2 and Motor3 are roughly $\frac{1}{0.7}$ times bigger than Motor1 and Motor4. The bigger thrust commands compensate the loss thrust of the defective motors after the feedback of the motors efficiency.

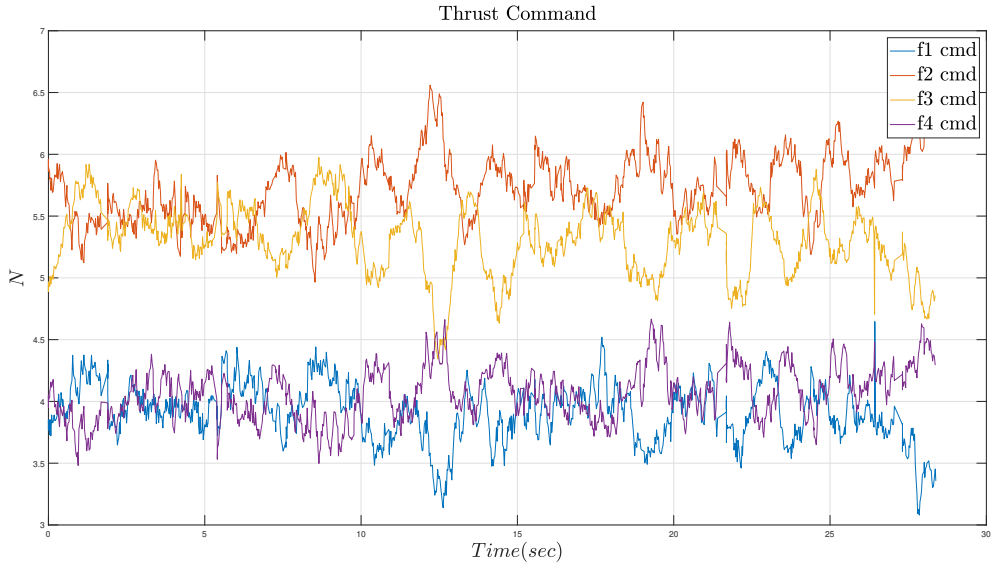


Figure 34: Thrust Command

7.2 The CTS

In this section, the CTS experimental control performance using developed controller are presented. The UKF estimator hasn't be verified through experiment because the force and

torque sensors haven't arrived yet.

7.2.1 Hardware Architecture

Two DJI F450 frame of multirotors are deployed as the hardware architecture to implement the developed controller in the experiments. XBee modules are equipped to both of multirotors to communicate between the multirotors and the ground station. Both of multirotors don't communicate with each other. Angular velocity and acceleration for obtaining the attitude of the multirotors are measured from inertial measurement unit (IMU) respectively, and the position of the CTS is measured from motion capture system (Optitrack) with 12 cameras. Noted that the position mark is placed on the payload, and both of multirotors receive only the CTS position instead of their own position respectively. The configuration of the CTS is shown in Fig. 35.

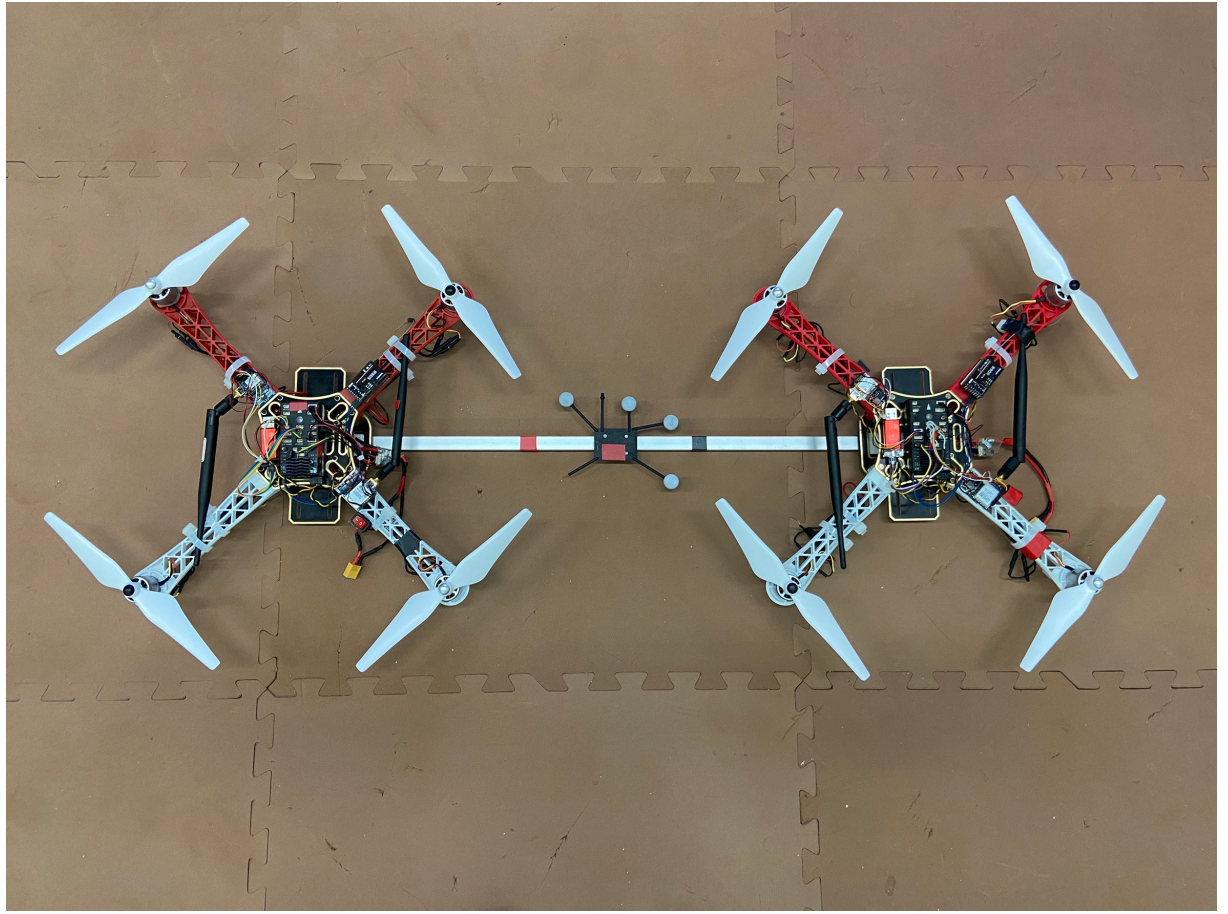


Figure 35: The CTS Hardware architecture.

The ground truth parameters, control gains, and parameters used in the developed controller are listed in Table 17, Table 18, respectively. The ground truth of moment of inertia was obtained by establishing the physical model of the multirotor in the Simscape environment and the ground

truth of mass was measured on the scales. The value of moment of inertia J_s , mass m_s and the distance between the multirotor and COM of the CTS r are represented in Table 17.

Table 17: Parameters used in the experiments

Parameter	Value	Unit
m_s	2.36	kg
J_s	$\text{diag}([0.395, 0.023, 0.410])$	$\text{kg} \cdot \text{m}^2$
r	0.403	m

Table 18: Control gains used in the experiments

Parameter	Value
$k_x + k_{xD}$	$\text{diag}([8, 12, 30])$
$k_v + k_{vD}$	$\text{diag}([2, 4.4, 12])$
$k_R + k_{RD}$	$\text{diag}([15, 5, 42.6])$
$k_\Omega + k_{\Omega D}$	$\text{diag}([1.4, 0.5, 2.94])$

7.2.2 Tracking Performance

After a minimum-snap trajectory being generated in Section. 7.1.2, we test our developed controller with two runs of the trajectory. The two dimensions heart trajectory tracking performance are presented in Fig. 36. In Fig. 36, the Desired Position line represents the position trajectory of the CTS and the Real Position line represents the experimental position trajectory of the CTS.

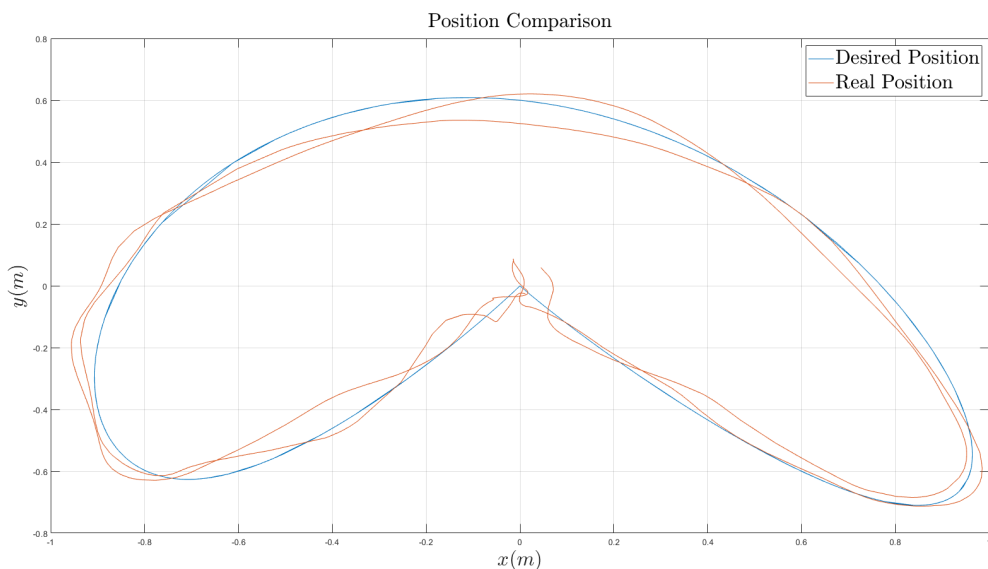


Figure 36: Tracking performance of the 2D position

Fig. 36 verifies that the CTS is be able to track a heart trajectory with the developed controller.

陽明交大
NYCU

Chapter 8 Conclusion

This research has developed the high gain geometric tracking controller with the feedback of the motors efficiency to controll a multirotor and the CTS under the influence of defective motors and the error of feedback motors efficiency estimated by UKF model ,and the developed controller can endure the disturbance caused by the defective motors and the error of the feedback motors efficiency. Though the defective motors lead to more translational and rotational error, the feedback estimated motors efficiency significantly reduce the error during flight. That is to say the performance of the flight is improved when the motors of the multirotor is defective and is proved in experiment. In addition, the controller stability analysis and the observability of the new designed UKF model observability is proved.

Future work will include removing the torque sensor applied in the CTS, and reducing the effect of unmodeled disturbance like wind, low battery voltage. The former can significantly reduce the cost of the CTS, the latter can get the more accurate estimation of the motors efficiency.



References

- [1] B. J. Brelje and J. R. Martins, “Electric, hybrid, and turboelectric fixed-wing aircraft: A review of concepts, models, and design approaches,” *Progress in Aerospace Sciences*, vol. 104, pp. 1–19, 2019.
- [2] G. A. Cardona, J. Ramirez-Rugeles, E. Mojica-Nava, and J. M. Calderon, “Visual victim detection and quadrotor-swarm coordination control in search and rescue environment,” *International Journal of Electrical and Computer Engineering*, vol. 11, no. 3, p. 2079, 2021.
- [3] T. Elmokadem, “Distributed coverage control of quadrotor multi-uav systems for precision agriculture,” *IFAC-PapersOnLine*, vol. 52, no. 30, pp. 251–256, 2019.
- [4] V. Chamola, P. Kotes, A. Agarwal, N. Gupta, M. Guizani *et al.*, “A comprehensive review of unmanned aerial vehicle attacks and neutralization techniques,” *Ad hoc networks*, vol. 111, p. 102324, 2021.
- [5] D. K. Villa, A. S. Brandao, and M. Sarcinelli-Filho, “A survey on load transportation using multirotor uavs,” *Journal of Intelligent & Robotic Systems*, vol. 98, no. 2, pp. 267–296, 2020.
- [6] L. Wang, “Pid control of multi-rotor unmanned aerial vehicles,” 2020.
- [7] M. S. Chehadeh and I. Boiko, “Design of rules for in-flight non-parametric tuning of pid controllers for unmanned aerial vehicles,” *Journal of the Franklin Institute*, vol. 356, no. 1, pp. 474–491, 2019.
- [8] C. Diao, B. Xian, Q. Yin, W. Zeng, H. Li, and Y. Yang, “A nonlinear adaptive control approach for quadrotor uavs,” in *2011 8th Asian Control Conference (ASCC)*. IEEE, 2011, pp. 223–228.
- [9] A. Parikh, R. Kamalapurkar, and W. E. Dixon, “Integral concurrent learning: Adaptive control with parameter convergence using finite excitation,” *International Journal of Adaptive Control and Signal Processing*, vol. 33, no. 12, pp. 1775–1787, 2019.

- [10] R. Xu and U. Ozguner, “Sliding mode control of a quadrotor helicopter,” in *Proceedings of the 45th IEEE Conference on Decision and Control*. IEEE, 2006, pp. 4957–4962.
- [11] H. Razmi and S. Afshinifar, “Neural network-based adaptive sliding mode control design for position and attitude control of a quadrotor uav,” *Aerospace Science and Technology*, vol. 91, pp. 12–27, 2019.
- [12] D. J. Almakhles, “Robust backstepping sliding mode control for a quadrotor trajectory tracking application,” *IEEE Access*, vol. 8, pp. 5515–5525, 2019.
- [13] X. He, G. Kou, M. Calaf, and K. K. Leang, “In-ground-effect modeling and nonlinear-disturbance observer for multirotor unmanned aerial vehicle control,” *Journal of Dynamic Systems, Measurement, and Control*, vol. 141, no. 7, 2019.
- [14] T. Lee, M. Leok, and N. H. McClamroch, “Geometric tracking control of a quadrotor uav on $\text{se}(3)$,” in *49th IEEE conference on decision and control (CDC)*. IEEE, 2010, pp. 5420–5425.
- [15] Z. Hou, P. Lu, and Z. Tu, “Nonsingular terminal sliding mode control for a quadrotor uav with a total rotor failure,” *Aerospace Science and Technology*, vol. 98, p. 105716, 2020.
- [16] Y.-H. Lien, C.-C. Peng, and Y.-H. Chen, “Adaptive observer-based fault detection and fault-tolerant control of quadrotors under rotor failure conditions,” *Applied Sciences*, vol. 10, no. 10, p. 3503, 2020.
- [17] W. Chung and H. Son, “Fault-tolerant control of multirotor uavs by control variable elimination,” *IEEE/ASME Transactions on Mechatronics*, vol. 25, no. 5, pp. 2513–2522, 2020.
- [18] H. A. Izadi, Y. Zhang, and B. W. Gordon, “Fault tolerant model predictive control of quadrotor helicopters with actuator fault estimation,” *IFAC Proceedings Volumes*, vol. 44, no. 1, pp. 6343–6348, 2011.
- [19] J. P. Ortiz, L. I. Minchala, and M. J. Reinoso, “Nonlinear robust h-infinity pid controller for the multivariable system quadrotor,” *IEEE Latin America Transactions*, vol. 14, no. 3, pp. 1176–1183, 2016.
- [20] Y. Zhong, Y. Zhang, W. Zhang, J. Zuo, and H. Zhan, “Robust actuator fault detection and diagnosis for a quadrotor uav with external disturbances,” *IEEE Access*, vol. 6, pp. 48 169–48 180, 2018.

- [21] Y. Zhong, W. Zhang, Y. Zhang, J. Zuo, and H. Zhan, “Sensor fault detection and diagnosis for an unmanned quadrotor helicopter,” *Journal of Intelligent & Robotic Systems*, vol. 96, no. 3, pp. 555–572, 2019.
- [22] B. Wang, Y. Shen, and Y. Zhang, “Active fault-tolerant control for a quadrotor helicopter against actuator faults and model uncertainties,” *Aerospace Science and Technology*, vol. 99, p. 105745, 2020.
- [23] A. Chamseddine, D. Theilliol, Y. Zhang, C. Join, and C.-A. Rabbath, “Active fault-tolerant control system design with trajectory re-planning against actuator faults and saturation: application to a quadrotor unmanned aerial vehicle,” *International Journal of Adaptive Control and Signal Processing*, vol. 29, no. 1, pp. 1–23, 2015.
- [24] F. Chen, R. Jiang, K. Zhang, B. Jiang, and G. Tao, “Robust backstepping sliding-mode control and observer-based fault estimation for a quadrotor uav,” *IEEE Transactions on Industrial Electronics*, vol. 63, no. 8, pp. 5044–5056, 2016.
- [25] O. Mofid and S. Mobayen, “Adaptive sliding mode control for finite-time stability of quadrotor uavs with parametric uncertainties,” *ISA transactions*, vol. 72, pp. 1–14, 2018.
- [26] M. Labbadi and M. Cherkaoui, “Robust adaptive nonsingular fast terminal sliding-mode tracking control for an uncertain quadrotor uav subjected to disturbances,” *ISA transactions*, vol. 99, pp. 290–304, 2020.
- [27] D. Mellinger, M. Shomin, N. Michael, and V. Kumar, *Cooperative Grasping and Transport Using Multiple Quadrotors*. Berlin, Heidelberg: Springer Berlin Heidelberg, 2013, pp. 545–558.
- [28] G. Welch, G. Bishop *et al.*, “An introduction to the kalman filter,” 1995.
- [29] M. I. Ribeiro, “Kalman and extended kalman filters: Concept, derivation and properties,” *Institute for Systems and Robotics*, vol. 43, p. 46, 2004.
- [30] E. A. Wan and R. Van Der Merwe, “The unscented kalman filter for nonlinear estimation,” in *Proceedings of the IEEE 2000 Adaptive Systems for Signal Processing, Communications, and Control Symposium (Cat. No. 00EX373)*. Ieee, 2000, pp. 153–158.

- [31] M. F. Beatty, “Kinematics of finite, rigid-body displacements,” *American Journal of Physics*, vol. 34, no. 10, pp. 949–954, 1966.
- [32] R. Hermann and A. Krener, “Nonlinear controllability and observability,” *IEEE Transactions on automatic control*, vol. 22, no. 5, pp. 728–740, 1977.
- [33] J.-M. Li, C.-W. Chen, and T.-H. Cheng, “Motion prediction and robust tracking of a dynamic and temporarily-occluded target by an unmanned aerial vehicle,” *IEEE Transactions on Control Systems Technology*, vol. 29, no. 4, pp. 1623–1635, 2020.
- [34] T. Lee, M. Leok, and N. H. McClamroch, “Geometric tracking control of a quadrotor UAV on $\text{SE}(3)$,” in *IEEE Conf. Decis. Control*, 2010, pp. 5420–5425.
- [35] D. Shevitz and B. Paden, “Lyapunov stability theory of nonsmooth systems,” *IEEE Trans. Autom. Control*, vol. 39 no. 9, pp. 1910–1914, 1994.
- [36] S. Documentation, “Simulation and model-based design,” 2022.
- [37] D. Mellinger and V. Kumar, “Minimum snap trajectory generation and control for quadrotors,” in *Proc. IEEE Int. Conf. Robot. Autom.*, 2011, pp. 2520–2525.